

The Nature and Origin of Low-Redshift O VI Absorbers

Benjamin D. Oppenheimer¹, Romeel Davé¹

¹*Astronomy Department, University of Arizona, Tucson, AZ 85721*

1 November 2018

ABSTRACT

The O VI ion observed in quasar absorption line spectra is the most accessible tracer of the cosmic metal distribution in the low redshift ($z < 0.5$) intergalactic medium (IGM). We explore the nature and origin of O VI absorbers using cosmological hydrodynamic simulations including galactic outflows with a range of strengths. We consider the effects of ionization background variations, non-equilibrium ionization and cooling, uniform metallicity, and small-scale (sub-resolution) turbulence. Our main results are (1) IGM O VI is predominantly photo-ionized with $T \approx 10^{4.2 \pm 0.2}$ K. A key reason for this is that O VI absorbers preferentially trace over-enriched (by $\sim \times 5$) regions of the IGM at a given density, which enhances metal-line cooling such that absorbers can cool to photo-ionized temperatures within a Hubble time. As such, O VI is not a good tracer of the Warm-Hot Intergalactic Medium. (2) The predicted O VI properties fit observables if and only if sub-resolution turbulence is added, regardless of any other model variations. The required turbulence increases with O VI absorber strength. Stronger absorbers arise from more recent outflows, so qualitatively this can be understood if IGM turbulence dissipates on the order of a Hubble time. The amount of turbulence is consistent with other examples of turbulence observed in the IGM and galactic halos. (3) Metals traced by O VI and H I do not trace exactly the same baryons, but reside in the same large-scale structure. Our simulations reproduce observed alignment statistics between O VI and H I, yet aligned absorbers typically have O VI arising from cooler gas, and for stronger absorbers lower densities, than H I. Owing to peculiar velocities dominating the line structure, coincident absorption often arises from spatially distinct gas. (4) Photo-ionized O VI traces gas in a variety of environments, and is not directly associated with the nearest galaxy, though is typically nearest to $\sim 0.1 L_*$ galaxies. Weaker O VI components trace some of the oldest cosmic metals. (5) Very strong absorbers ($EW \gtrsim 100 \text{ m\AA}$) are more likely to be collisionally ionized, tracing more recent enrichment ($\lesssim 2$ Gyr) within or near galactic halos.

Key words: intergalactic medium, galaxies: evolution, cosmology: theory, methods: numerical

1 INTRODUCTION

The exploration of metals in the low redshift ($z < 0.5$) intergalactic medium (IGM) has taken a large leap forward with the advent of high-resolution space-based ultraviolet (UV) spectroscopy with the *Hubble Space Telescope Imaging Spectrograph* (STIS) and *Far Ultraviolet Spectroscopic Explorer* (FUSE). The strongest and most common metal transition seen in quasar absorption line spectra is the O VI doublet at 1032,1038Å. Many recent papers (e.g. Tripp & Savage 2000; Savage et al. 2002; Prochaska et al. 2004; Richter et al. 2004; Sembach et al. 2004a; Lehner et al. 2006; Cooksey et al. 2008) have examined O VI absorbers along single sight lines, and have fit ionization models to individual systems with associated Ly α

and lower ionization metal transitions. Three recent studies (Tripp et al. 2008, hereafter T08; Danforth & Shull 2008, hereafter DS08; and Thom & Chen 2008a, 2008b) have compiled samples of O VI, providing the largest statistical surveys to date.

Understanding O VI in the low- z Universe is extremely important, because it may hold the key to locating a significant reservoir of cosmic baryons and metals (e.g. Tripp et al. 2000). The inventory of observed baryons (e.g. Fukugita et al. 1998) falls well short of the predicted cosmological values from the cosmic microwave background (Hinshaw et al. 2008), leading to the well-known “missing baryons problem.” Cosmological simulations (Cen & Ostriker 1999; Davé et al. 1999, 2001) sug-

gest that a large fraction of baryons today ($> 30\%$) reside in a hard-to-observe warm-hot intergalactic medium (WHIM), with temperatures of $T = 10^5 - 10^7$ K. The WHIM results primarily from shocks created during large-scale structure formation. More recent simulations including feedback (Cen & Ostriker 2006; Oppenheimer & Davé 2008, hereafter OD08) find that galactic winds may increase the fraction of cosmic baryons in the WHIM to 50% or more.

A possibly related problem is that only $\frac{1}{3}$ of metals have been accounted for observationally (Fukugita & Peebles 2004), judging from the mismatch between the amount of metals nucleosynthesized and ejected by observed stars and those observed in various cosmic baryonic components. O VI potentially represents the Holy Grail of all things missing in the low- z Universe, because its collisionally ionized equilibrium (CIE) maximum temperature, $10^{5.45}$ K, provides a unique and relatively easily accessible tracer of WHIM metals and baryons. The incidence of O VI with broad Ly α absorbers (BLAs) thought to trace gas at $T > 10^5$ K (e.g. Richter et al. 2004) supports this notion, while O VI seen with very broad H I having line widths > 100 km s $^{-1}$ may indicate even hotter O VI at $T \sim 10^6$ K (e.g. Danforth et al. 2006).

Early investigations into O VI using cosmological simulations (Cen et al. 2001; Fang & Bryan 2001; Chen et al. 2003) predicted that stronger O VI absorbers tend to be collisionally ionized while weaker ones tend to be photo-ionized, with the cross-over equivalent width of $\sim 30 - 50$ mÅ. Cen & Fang (2006) added non-equilibrium ionization and used higher resolution simulation, finding similar behavior compared to their earlier work. The above simulations generally focused on fitting only the observed cumulative equivalent width (EW) distribution. Recent observations now provide new challenges for simulations to fit a wider range of low- z O VI observables.

Recent surveys have renewed confusion about the nature of O VI absorbers. Ionization models for absorbers showing aligned O VI, H I, and C III are usually forced to invoke multi-phase gas, with both O VI in CIE and lower ionization species at photo-ionized temperatures (Prochaska et al. 2004; Danforth et al. 2006; Cooksey et al. 2008). Yet T08 find that the majority of aligned H I – O VI absorbers can also be explained by photo-ionization alone. The “blind” searches of O VI without H I by Thom & Chen (2008a) indicate $\gtrsim 95\%$ of O VI is associated with H I. These studies suggest that O VI traces baryons at least partially accounted for by H I absorbers, and is not necessarily a good tracer of the WHIM. Studies of galaxy-absorber correlations find a wide variety of environments for O VI absorbers including voids, filaments, galaxies, and groups (e.g. Tripp et al. 2001; Tumlinson et al. 2005; Prochaska et al. 2006; Tripp et al. 2006). Furthermore, it is not clear how the O VI in intermediate- and high-velocity clouds (IVCs and HVCs) associated with the Milky Way (MW) halo (e.g. Sembach et al. 2003; Savage et al. 2003; Fox et al. 2005) relate to O VI observed in quasar absorption line spectra. A unified model was proposed by Heckman et al. (2002) where O VI absorbers are all radiative cooling flows passing through the coronal temperature regime, with a modification by Furlanetto et al. (2005) for long cooling times in the IGM. However, observations are inconclusive as to whether this scenario also applies to IGM O VI (e.g. Danforth et al. 2006;

Lehner et al. 2006). Hence there remains much uncertainty in regards to which cosmic gas and metal phases O VI absorbers actually trace.

In this paper we explore O VI and H I absorbers in a range of physical models using our modified version of the cosmological hydrodynamics code GADGET-2. We pay close attention to three key observables confirmed in multiple studies: the cumulative EW distribution, O VI linewidths (b -parameters) as a function of O VI column density, and the alignment of O VI with H I. Our two main goals are (1) to see how self-consistent metal enrichment via galactic superwinds reproduces the O VI observations, including an honest evaluation of the short-comings of our simulations, and (2) to understand the physical conditions and environments of O VI absorbers. This study combines state-of-the-art modeling with the most recent O VI data to further understand the nature of IGM O VI, in light of the much anticipated installation of the *Cosmic Origins Spectrograph* (COS) and the re-activation of STIS on *Hubble*.

The structure of the paper flows as follows. In §2, we introduce our simulations all run to $z = 0$ with three different galactic outflow models, plus other post-run input physics variations. Then, in §3 we see how the various models fit the Ly α forest and our three O VI observables, including a test of resolution convergence. The crux of this paper lies in the following sections where we dissect our simulated absorber population, acknowledging the imperfections in our modeling while assessing what we believe is physically significant. §4 advocates that IGM O VI absorbers are primarily photo-ionized, with an in-depth analysis of the association with H I, and forwards an explanation for the non-thermal component of O VI line profiles as arising from small-scale turbulence. §5 examines the origin of O VI absorbers with an emphasis on environment. We discuss the minority population of collisionally ionized O VI here, and examine tell-tale signs of such WHIM absorbers with an eye towards COS. We summarize in §6.

Throughout this paper, we adopt Asplund et al. (2005) solar abundances, as most low- z O VI observations use this or a similar value. This contrasts to our use of Anders & Grevesse (1989) values in previous publications (Oppenheimer & Davé 2006, hereafter OD06; Davé & Oppenheimer 2007; OD08), and results in a significant decrease in solar oxygen mass fraction (0.00541 versus 0.00962). The Type II supernovae (SNe) yields we use as simulation inputs are from Limongi & Chieffi (2005), and are independent of solar values. For ease of discussion, we classify O VI absorbers into three categories according to their column density: weak ($N(\text{O VI}) < 10^{13.5}$ cm $^{-2}$), intermediate ($N(\text{O VI}) = 10^{13.5-14.5}$ cm $^{-2}$), and strong ($N(\text{O VI}) = 10^{14.5-15.0}$ cm $^{-2}$). We often split the intermediate absorbers into two bins, since this comprises the majority of observed O VI.

2 SIMULATIONS

We use cosmological simulations run to $z = 0$ using our modified version of the N-body + Smoothed Particle Hydrodynamics code GADGET-2 (Springel 2005) in order to explore the nature of O VI in the low- z Universe. Our simulations directly account for cosmic metal enrichment via enriched galactic outflows, where outflow parameters are tied to

galaxy properties following that observed in local starbursts. Our most successful model follows scalings for momentum-driven winds; this fairly uniquely matches a wide range of observations such as early IGM enrichment (OD06), the galaxy mass-metallicity relations (Finlator & Davé 2008), and the enrichment and entropy levels seen in intragroup gas (Davé et al. 2008). We introduce the simulations first, then describe variations applied to our favored outflow model, and finally describe post-run variations to the input physics.

2.1 Model Runs

Our simulations adopt cosmological parameters based on 5-year WMAP results (Hinshaw et al. 2008). The parameters are $\Omega_0 = 0.25$, $\Omega_\Lambda = 0.75$, $\Omega_b = 0.044$, $H_0 = 70$ km s⁻¹ Mpc⁻¹, $\sigma_8 = 0.83$, and $n = 0.95$; we refer to this as the *d*-series. The value of σ_8 is slightly higher than favored from WMAP data alone, but it agrees better with combined results from Type Ia SNe and baryon acoustic oscillation data. Our general naming convention is `d[boxsize]n[particles/side][wind model]`.

We use the momentum-driven wind model based on the analytic derivation by Murray, Quatert, & Thompson (2005) and explored previously in OD06 and OD08. Briefly, wind velocity (v_{wind}) scales linearly with the galaxy velocity dispersion (σ), and mass loading factor (η) scales inversely with σ . The mass loading factor represents the mass loss rate in outflows in units of the galaxy star formation rate. We use the following relations for v_{wind} and η :

$$v_{\text{wind}} = 3\sigma\sqrt{f_L - 1}, \quad (1)$$

$$\eta = \frac{\sigma_0}{\sigma}, \quad (2)$$

where f_L is the luminosity factor in units of the galactic Eddington luminosity (i.e. the critical luminosity necessary to expel gas from the galaxy potential), and σ_0 is the normalization of the mass loading factor. A minor difference from OD06 and OD08 is that we no longer impose an upper limit on v_{wind} due to SN energy limitations.

The model runs, detailed in Table 1, have [*wind model*] suffixes denoting a variation of the momentum-driven wind model run. Our previously used favored model, *vzw*, contains a spread in $f_L = 1.05 - 2.00$, includes a metallicity dependence for f_L owing to more UV photons output by lower-metallicity stellar populations, and adds an extra boost to get out of the galaxy potential well simulating continuous acceleration by UV photons.

Figure 1 illustrates a 25 km s⁻¹ slice spanning the full extent of the d32n256vzw150 simulation box at $z = 0.25$. The location of galaxies (upper left) is well correlated with the enriched IGM (upper right). The Ly α forest traces baryons in filaments (bottom left) down to the lowest observable column densities. The OVI absorbers (bottom right) mainly trace the diffuse IGM enriched via feedback, showing a more grainy structure indicative of inhomogeneous enrichment. Much of this paper focuses on quantifying the relationship between these various observational and physical components of the IGM.

We run 16 and 32 h^{-1} Mpc (comoving) sized boxes at the same mass and spatial resolution (with different numbers of particles) of this wind model. The baryon fraction in stars

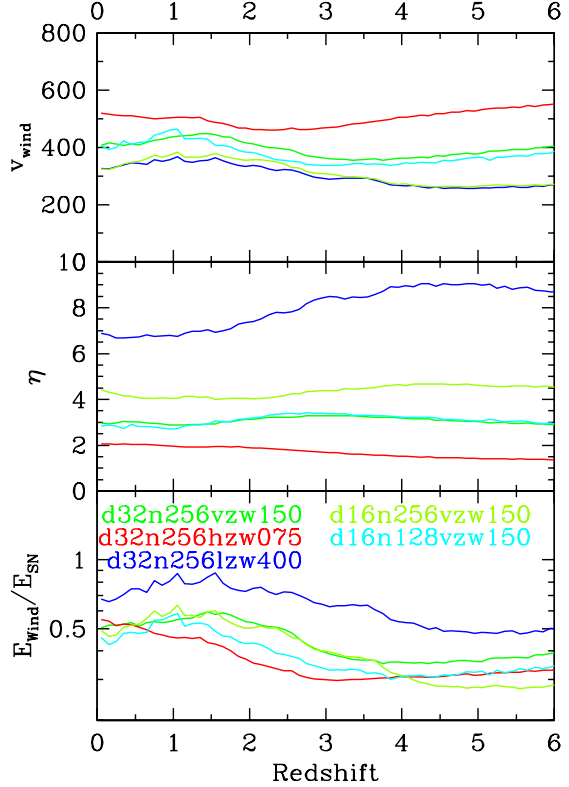


Figure 2. Wind properties as a function of redshift for our three wind models, plus one higher resolution simulation (d16n256vzw150), and a simulation to test box size convergence (d16n128vzw150). In order to create a reasonable baryonic fraction in stars at $z = 0$, weaker winds (top panel) must have a higher mass loading factor (middle panel) resulting in greater energy input per unit star formation as shown by the $E_{\text{wind}}/E_{\text{SN}}$ ratio (lower panel). The opposite applies for the *lzw* model. E_{SN} is set to 1.3×10^{49} ergs M_\odot^{-1} .

is identical, while the wind speed and mass loading shown in Figure 2 are in good agreement from $z = 6 \rightarrow 0$, despite a volume difference of $8\times$ (compare green vs. cyan lines). $E_{\text{wind}}/E_{\text{SN}}$ decreases slightly in the smaller volume, because fewer massive galaxies having higher wind energy efficiencies form at early times.

We also run a $16h^{-1}$ Mpc box length, 2×256^3 particle simulation to $z = 0$ (d16n256vzw150) to explore resolution convergence. This run with its smaller time stepping is the most computationally expensive run, using over 30,000 CPU hours on Harpertown Intel Xeon processors. The wind properties in Figure 2 indicate lower v_{wind} 's and higher η 's due to increased contributions from small galaxies below the resolution limit of the d32n256vzw150 box. The stellar baryon fraction is 4% higher in this simulations, mainly due to late time star formation. We suspect this is due to the non-cosmological scale of this box, which cannot form as many groups and clusters at late times where star formation is inhibited, as well as the fact that it probes further down the relatively steep mass function of star-forming galaxies.

In this paper we explore two other variations of the momentum-driven wind model that bookend, at high and low wind speeds, physically plausible winds that are able to enrich the IGM as observed. In addition to varying v_{wind} ,

Table 1. Simulations

Name ^a	L^b	ϵ^c	m_{SPH}^d	Wind Model	σ_0^e	$\Omega_*/\Omega_b(z=0)^f$
d32n256vzw150	32	2.5	34.6	Momentum-driven	150	0.102
d16n128vzw150	16	1.5	34.6	“	150	0.144
d16n256vzw150	16	1.25	4.31	“	150	0.144
d32n256hzw075	32	2.5	34.6	Hybrid Momentum-SNe	75	0.061
d32n256lzw400	32	2.5	34.6	Low- v_{wind} Momentum	400	0.116

^a *vzw* suffix refers to the momentum-driven winds. *hzw* suffix refers to momentum-driven winds with an added boost from SNe. *lzw* suffix refers to momentum-driven winds launched with 51% as much kinetic energy relative to *vzw*.

All models are run to $z = 0$

^b Box length of cubic volume, in comoving $h^{-1}\text{Mpc}$.

^c Equivalent Plummer gravitational softening length, in comoving $h^{-1}\text{kpc}$.

^d Masses quoted in units of $10^6 M_\odot$.

^e Normalization for the momentum-driven wind mass-loading factor where $\eta = \sigma_0/\sigma$, units in km s^{-1} .

^f Fraction of baryons in stars.

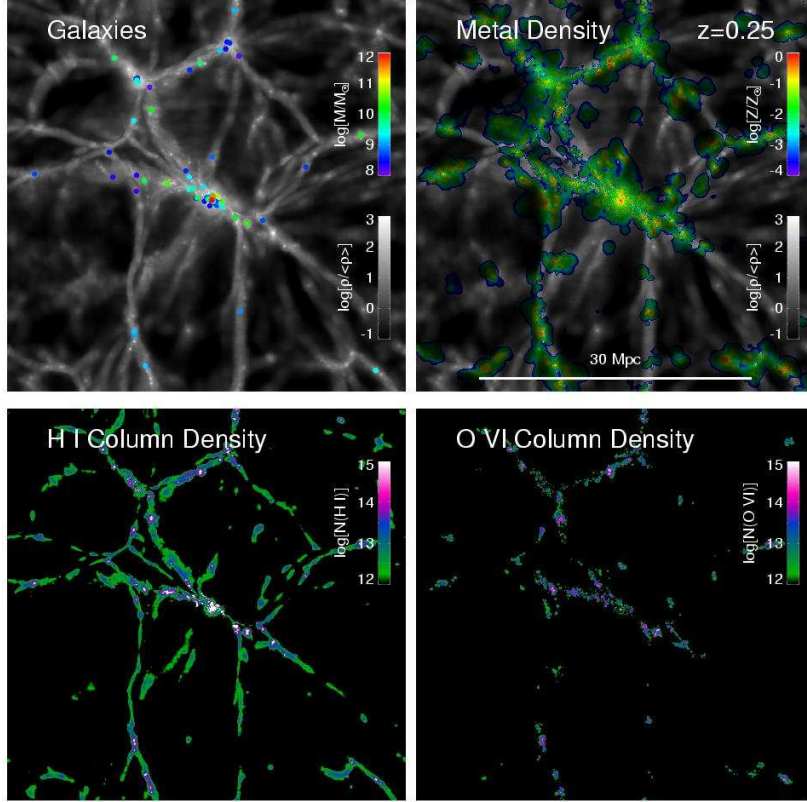


Figure 1. A 25 km s^{-1} slice of IGM spanning the 32 comoving $h^{-1}\text{Mpc}$ of the d32n256vzw150 simulation at $z = 0.25$. *Upper left:* The locations of galaxies are shown as colored points, where the color corresponds to stellar mass, overlaid on the gas overdensity represented in greyscale. *Upper right:* Color indicates the enrichment level; 90% of the IGM remains unenriched as the superwinds are unable to enrich voids. *Bottom panels:* H I (left) and O VI (right) column densities in this 25 km s^{-1} slice, assuming a uniform Haardt & Madau (2001) ionization background. O VI is not as extended as H I, partially due to the small volume filling factor of metals, however the strongest O VI absorbers are often found associated with sub- M^* galaxies, unlike H I, which has its strongest absorption around the large group in the center. The vast majority of O VI in our simulations is photo-ionized tracing overdensities of 10-200.

we must also vary σ_0 to match the observed baryon fraction in stars today of $\sim 6 - 10\%$ (Cole et al. 2001).

The high- v_{wind} case is denoted *hzw* in which a portion of the energy from Type II SNe is used to increase v_{wind} , while keeping the momentum-driven wind derived η the same. We use $1.9 \times 10^{48} \text{ erg } M_\odot^{-1}$, or one-seventh of the total supernova

energy from a Chabrier IMF, assuming each star between $8 - 100 M_\odot$ explodes with 10^{51} ergs. Additionally, we add $1.9 \times 10^{48} \text{ erg } M_\odot^{-1}$ of SNe energy to the thermal energy of each wind particle, and allow adiabatic expansion (i.e. no cooling) while the wind particle is hydrodynamically decoupled.

The *hzw* model is designed to explore the case where

we push feedback to extreme physical limits with the specific purpose to see if such strong feedback can make IGM metals both more widely distributed and hotter in the low- z Universe. In order to obtain a reasonable stellar density by low- z we set $\sigma_0 = 75 \text{ km s}^{-1}$, which results in 6.1% of baryons in stars at $z = 0$. Figure 2 shows the wind parameters as a function of redshift. Ironically, the lower η of the *hzw* model reduces the efficiency of winds as indicated by the lowest $E_{\text{wind}}/E_{\text{SN}}$ ratio of all three wind models explored.

To explore the low- v_{wind} case, we run the *lzw* model in which the wind velocity is reduced by 50% relative to the *vzw* model. In order to prevent the formation of too many stars by $z = 0$, σ_0 is set to 400 km s^{-1} , resulting in $\Omega_*/\Omega_b = 0.103$ at $z = 0$. The *lzw* model generates the most wind energy per baryonic mass ($E_{\text{wind}}/E_{\text{SN}}$), because of the high mass loading factor.

2.2 Post-Run Physics Variations

A variety of post-run treatments are performed on the model runs, using modifications within our quasar absorption line spectral generator, *specexbin*. Some of these variations are used to explore the consequences of unlikely but intuitive scenarios (i.e. a uniform metallicity distribution), while others are meant to account for physics not included in our simulations (i.e. non-equilibrium ionization). We list these variations below, and denote such model variations throughout the text with an additional suffix at the end of the model name.

Z01: This model variation uses a uniform metallicity of $0.1 Z_{\odot}$ for every SPH particle instead of the metallicity from the simulation. This unrealistic model presents an exercise to see how O VI observations vary if metals are uniformly distributed. $0.1 Z_{\odot}$ is the fiducial value that was needed in early simulation studies to match the equivalent width distribution of low- z O VI absorbers (Cen et al. 2001; Fang & Bryan 2001; Chen et al. 2003). It is also similar to the average $z = 0$ oxygen content of the d32n256vzw150 simulation, $0.13 Z_{\odot}$. We do not alter the gas densities or temperatures, so the ionization conditions remain the same.

ibkgd: By default, we use a spatially uniform ionization background given of Haardt & Madau (2001) background, *with* a contribution from quasars *and* star forming (SF) galaxies (10% escape fraction) included. We use the normalization taken directly from Haardt & Madau (2001) with no adjustment, since as we will show this reproduces $z \sim 0$ Ly α forest statistics quite well (see also Paschos et al. 2008). The hydrogen photo-ionization rate is $\Gamma = 1.84 \times 10^{-13} \text{ s}^{-1}$ at $z = 0.25$. To explore variations in photo-ionization, we consider two other uniform ionization backgrounds:

1. *ibkgd-Q1* uses intensity from the Haardt & Madau (2001) background, minus the contribution from SF galaxies. This mainly affects H I properties as SF galaxies contribute $\sim \frac{2}{3}$ of the ionization at the Lyman limit, therefore the absorption from the Ly α forest will grow. The ionization intensity at the O VI ionization potential, 8.4 Rydbergs, remains mostly unaffected by subtracting star forming galaxies. This background may be applicable in regions where the mean free paths of H I ionizing photons are shorter than O VI ionizing photons, e.g. denser regions in and around galactic haloes.
2. *ibkgd-Q3* uses triple the quasar-only Haardt & Madau (2001) background, which better reproduces the global

statistics of the Ly α forest. There are now more photons at 8.4 Rydberg, which leads to photo-ionized O VI at higher overdensities. We explore this alternative since little is known about the true ionization field at these high energies.

noneq: Our default case assumes ionization equilibrium for all species, which we calculate using CLOUDY (Ferland et al. 1998). To test sensitivity to this assumption for collisionally ionized O VI, we apply the non-equilibrium ionization tables of Gnat & Sternberg (2007) as a function of temperature and metallicity rather than our CLOUDY-generated equilibrium tables. Gnat & Sternberg (2007) calculated non-equilibrium ionization fractions as a function of metallicity assuming collisional ionization only. High-metallicity shocked gas cools more rapidly than it can recombine, resulting in higher ionization states than expected at lower temperatures when assuming CIE. This has implications for O VI at densities where it is collisionally ionized, because ionization fractions of a few percent for O VI can exist at well below its CIE peak at $10^{5.45} \text{ K}$ if the gas is Z_{\odot} or above. There does not exist a non-equilibrium treatment for photo-ionized gas as of yet, since this depends additionally on density; however these ionization fractions are more likely to be regulated by the intensity of the ionization background. Ideally it would be best to directly include non-equilibrium ionization as in Cen & Fang (2006), but we leave that for future work, and consider this test as bracketing the plausible impact of non-equilibrium ionization.

To more fully explore the impact of non-equilibrium ionization, we also run a d16n128hzw075 simulation with the Gnat & Sternberg (2007) cooling tables as a function of metallicity. The metal line cooling peaks for individual ions are spread out over larger temperature ranges as individual ion coolants exist over a broader swath of temperature. The cooling is also of the order $2\text{--}4\times$ less in some places than Sutherland & Dopita (1993), because ion coolants exist at lower temperatures where they collide less rapidly. This run is denoted as d16n128hzw075-noneq. To ensure that this volume is not too small, we run a d16n128vzw150 simulation and find general convergence with d32n256vzw150 for the star forming, wind, and IGM enrichment properties; therefore this box size should be sufficient for comparison with larger volumes.

bturb: The most critical post-run modification we employ is the by-hand addition of sub-resolution turbulence. As we will show, our simulations do not reproduce the broadest observed absorption lines, especially those with $N(\text{O VI}) > 10^{14} \text{ cm}^{-2}$. Often, where observations see one broad component, our simulations would show a number of narrow components in a system. This is understandable when one considers our simulations have a mass resolution of $\bar{m}_{\text{SPH}} \approx 3.5 \times 10^7 M_{\odot}$, and metals may exist in structures of significantly smaller scale (e.g Rauch et al. 1999; Simcoe et al. 2006; Frank et al. 2007; Hao et al. 2007; Schaye et al. 2007). Even at the best-available instrumental resolution of STIS, thermal broadening at CIE O VI temperatures cannot explain the bulk of the line widths in the T08 dataset. Furthermore, the alignment with H I suggests that some non-thermal broadening mechanism is needed. Turbulence is often used as the overarching explanation (e.g. Thom & Chen 2008b). We will argue that O VI absorbers,

especially strong ones, are likely to be made up of numerous smaller metal concentrations with a range of velocities resulting in a component dominated by turbulent broadening.

We add turbulence residing on scales below the SPH particle resolution (“sub-SPH turbulence”) by adding a turbulent b -parameter as a function of hydrogen density (n_{H}). With no physical guide available, we add just enough turbulence to approximately match the observed line width distribution as a function of column density. Specifically, we apply a linear fit to the STIS-only sample of T08 $b(\text{O VI}) - N(\text{O VI})$ relation between $10^{12.9} - 10^{14.9} \text{ cm}^{-2}$ ($b_{\text{obs}} = 21.40 \times \log[N(\text{O VI})] - 268.4 \text{ km s}^{-1}$), and subtract our relation from the d32n256vzw150 lines of sight at STIS resolution ($b_{\text{noturb}} = 1.50 \times \log[N(\text{O VI})] - 8.9 \text{ km s}^{-1}$), using the equation

$$b_{\text{turb}}^2 = b_{\text{obs}}^2 - b_{\text{noturb}}^2. \quad (3)$$

b_{turb} is the turbulent broadening describing the small-scale motions within an SPH particle for this specific simulation resolution. We cast b_{turb} in terms of n_{H} by employing the relation

$$\log[n_{\text{H}}] = 0.66 \times \log[N(\text{O VI})] - 13.98 \text{ cm}^{-3}, \quad (4)$$

which is a dependence we find in §4.1. Putting it together, the relation we use in `specexbin` is

$$b_{\text{turb}} = \sqrt{1405 \log[n_{\text{H}}]^2 + 15674 \log[n_{\text{H}}] + 43610} \text{ km s}^{-1}, \quad (5)$$

applied only over the range $n_{\text{H}} = 10^{-5.31} - 10^{-4.5} \text{ cm}^{-3}$, describing the majority of O VI within filaments but outside galactic halos.

Since the sub-SPH turbulence from Equation 5 would extrapolate to artificially high values at higher densities, we use two more observational constraints from the O VI surveys of MW IVCs and HVCs to describe sub-SPH turbulence associated with galactic halos. Sembach et al. (2003) finds high-velocity O VI features have $b(\text{O VI}) = 40 \pm 14 \text{ km s}^{-1}$, and suggest this O VI arises between the interfaces of cool/warm clouds and the $T > 10^6 \text{ K}$ galactic corona/intragroup medium at $R > 70 \text{ kpc}$ with $n < 10^{-4} - 10^{-5} \text{ cm}^{-3}$. We assume that these lines are predominantly turbulently broadened, as temperature and spatial explanations fall well short, requiring another broadening mechanism possibly related to the motion of the gas (Sembach et al. 2003). If the absorption arises from CIE O VI ($T \sim 10^{5.5} \text{ K}$) then $n_{\text{H}} \approx 10^{-4.5} \text{ cm}^{-3}$ applies for this gas assuming approximate pressure equilibrium with the galactic corona. Therefore $b_{\text{turb}} \sim 40 \text{ km s}^{-1}$ corresponds to $n_{\text{H}} = 10^{-4.5} \text{ cm}^{-3}$ both in Equation 5 and in HVCs.

Savage et al. (2003) find $b(\text{O VI}) \approx 60 \text{ km s}^{-1}$ in IVCs, which they find most likely reside in the galactic thick disk with O VI densities tracing $n_{\text{H}} \sim 10^{-3} \text{ km s}^{-1}$ for O VI flows. Using a linear interpolation with these two constraints, we find the relation

$$b_{\text{turb}} = 13.93 \log(n_{\text{H}}) + 101.8 \text{ km s}^{-1} \quad (6)$$

for $n_{\text{H}} = 10^{-4.5} - 10^{-3.0} \text{ cm}^{-3}$, and assume a maximum $b_{\text{turb}} = 60 \text{ km s}^{-1}$ for higher densities. Very rarely do our random sight lines intersect densities as high as $n_{\text{H}} = 10^{-3} \text{ cm}^{-2}$, but such dense regions can create a strong absorption profile.

At $z = 0.25$, the sub-SPH turbulent broadening is $b_{\text{turb}} = 13, 22, 40$, and 51 km s^{-1} at $\rho/\bar{\rho} = 20, 32, 100$, and

320 respectively. Besides producing wider lines, it turns out to also help explain various other observed O VI absorber properties, as we show in §4.4.

3 SIMULATED VS. OBSERVED O VI AND H I ABSORBERS

In this section we place constraints on our models from observations of the low- z Ly α and O VI forests. We begin with the Ly α forest, considering column density and line width distributions, and the evolution from $z = 1.5 \rightarrow 0$. We then focus on three key O VI observables: (1) the cumulative equivalent width distribution, (2) $b(\text{O VI})$ as a function of $N(\text{O VI})$, and (3) the $N(\text{O VI})$ as a function of $N(\text{H I})$. We explore how each of our models fits these observables, and explain why models the turbulent broadening provide the best fit. We end the section discussing numerical resolution convergence among our simulations.

We generate 30 continuous lines of sight from $z = 1 \rightarrow 0$ shot at a variety of angles through each simulation using `specexbin`. We use a continuum-normalized spectral template with 0.02 \AA bins convolved with the STIS instrumental resolution (7 km s^{-1}), and add Gaussian noise with $S/N = 10$ per pixel. This creates a large sample of high quality spectra covering $\Delta z = 15$, larger than observational samples, with the intention to extract subtle differences between our various models. For the sake of simplicity, we generate H I-only and O VI-only spectra using only the strongest transition (i.e. Ly- α and the 1032 \AA line). See §2.5 of OD06 for a more detailed description of `specexbin`. The AutoVP package (Davé et al. 1997) is used to fit all component absorption lines, yielding e.g. a sample of 475 O VI components with $N(\text{O VI}) \geq 10^{13} \text{ cm}^{-2}$ in the d32n256vzw150-bturb model.

3.1 H I observables

The observationally well-characterized Ly α forest provides baseline constraints on our simulations. A successful model of O VI absorbers must first reproduce observations of the low- z Ly α forest, especially given that O VI is usually associated with H I absorption (Thom & Chen 2008a). The Ly α forest traces the warm photo-ionized IGM (i.e. $T \sim 10^4 \text{ K}$), which contains $\sim 30\%$ of cosmic baryons (Penton et al. 2004) and likely traces some of the same gas as photo-ionized O VI absorbers. We examine briefly three key H I observables spanning a range of physical and evolution properties that our simulations must match.

Figure 3 shows the column density distribution (left), evolution of line densities from $z = 1 \rightarrow 0$ (middle), and the $N - b$ relation (right) from observations and four of our simulations, namely d32n256vzw150, d16n256vzw150, d32n256vzw150-bturb, d32n256hzw075. We display only these models because there exist only minor differences in the Ly α forest amongst the other models. The comparison to data shows reasonably good agreement, except for an underestimate by at least a factor of two of strong H I lines ($EW > 240 \text{ m\AA}$). There are two likely reasons for this: The first is that the observations compared to have lower signal-to-noise and/or resolution than our simulated spectra, so

line blending may artificially enhance the observed equivalent widths; and second, many of these lines arise from gas within galactic haloes, where we may not be resolving halo substructures adequately. We note however that the higher resolution in the d16n256vzw150 simulation does little to resolve this discrepancy, so either we need much higher resolution or else line blending issues are important.

We find the low- z Ly α forest is relatively unaffected by wind strength; this is similar to the findings of Bertone & White (2006) at high- z , who find galactic winds do very little to alter the main statistical properties of the $z \sim 3$ Ly α forest. The only difference worth noting is that the strong winds of the hzw reduce the frequency of strong H I lines ($EW > 240$ mÅ) by about $\sim 20\%$.

We now compare our baseline vzw model with and without turbulence, since we will later show that the d32n256vzw150-bturb model best fits the O VI observables, and we want to quantify how sub-SPH turbulence influences the Ly α forest. Ideally, turbulence should not affect Ly α observables significantly since the low- z Ly α -forest is well-described by simulations without any added turbulence (Davé et al. 1999), and the b -parameters are well-described primarily by thermal and Hubble broadening (Davé & Tripp 2001).

The left panel shows the differential H I column density distribution, i.e. the number of absorbers per H I column density interval per redshift pathlength $d^2n/dN(\text{H I})dX$, from our models compared to power law fits by Penton et al. (2004, dashed line, $z = 0.002 - 0.069$) and Lehner et al. (2007, dotted line, $z < 0.4$). The different models show little variation from each other below $N(\text{H I}) = 10^{14} \text{ cm}^{-2}$, agreeing well with the slightly steeper power law of the Lehner et al. (2007) fit ($d^2n/dN(\text{H I}) \propto N(\text{H I})^{-1.83}$) over the same redshift interval. We use fits to Ly β for $N(\text{H I}) \geq 10^{14.4} \text{ cm}^{-2}$ absorbers, but find no statistical difference versus using only Ly α for the frequency of strong lines fit with AutoVP. We find fewer higher column density lines than observed (as also indicated by our comparison to the dN/dz of high equivalent width lines), but we note that an observer typically climbs up the Lyman series to fit the strongest lines resulting in a more accurate fit.

We consider the redshift evolution of Ly α absorbers in the central panel of Figure 3. The evolution is rapid down to $z \sim 2$ but slows significantly below $z \sim 1$ (Bahcall et al. 1991; Impey et al. 1996; Weymann et al. 1998), due to a decreasing ionization field strength counter-balancing decreasing rates of recombination due to Hubble expansion (Davé et al. 1999). Matching this trend is important, because the lack of evolution in H I may well be reflected in O VI. In this paper we do not explore O VI evolutionary trends, leaving it for future work, but we broadly find a comparable amount of evolution as in H I. We count the frequency of lines, dN/dz , for intermediate ($240 > EW \geq 60$ mÅ, $N(\text{H I}) = 10^{13.1-14.0} \text{ cm}^{-2}$) and strong absorbers ($EW \geq 240$ mÅ, $N(\text{H I}) = 10^{14.0-17.0} \text{ cm}^{-2}$). Our simulated intermediate absorbers agree with the evolution from higher z (Janknecht et al. 2006) to the local Universe (Penton et al. 2004). We do not calibrate the factor of two mismatch in stronger absorbers, because this more likely has to do with unresolved halo substructure and the breakdown of the optically thin assumption of the ionization background in such

regions; this is beyond the scope of this paper, and is not very relevant to the bulk of O VI absorbers, as it turns out.

The rightmost panel of Figure 3 shows the $b(\text{H I})$ - $N(\text{H I})$ correlation, with $1\text{-}\sigma$ dispersions, compiled from a number of quasar sight lines by Lehner et al. (2007). Our absorbers show a slow but steady increase until $N(\text{H I}) = 10^{14} \text{ cm}^{-2}$. Above $N(\text{H I}) > 10^{14.4} \text{ cm}^{-2}$, fitting to Ly β rather than Ly α avoids saturation effects, and yields systematically smaller b -parameters in AutoVP. The Lehner et al. (2007) sample combines FUSE and STIS data, and could result in different b -parameters than our uniform simulated STIS spectra (with typically higher S/N). The turbulent broadening starts making an impact in H I lines with $N(\text{H I}) \gtrsim 10^{14.0} \text{ cm}^{-2}$, tracing overdensities around 30, although it is not obvious whether the agreement with data is improved or worsened. A detailed comparison must wait for when the simulated spectra are generated and analyzed identically to observations.

An important marker of WHIM gas is broad Ly α absorbers (BLAs). Ideally, we would like to derive the frequency of BLAs since they are often thought to trace the same WHIM gas as collisionally ionized O VI (e.g. Richter et al. 2004). However, continuum fitting uncertainties, spectral resolution, and S/N sensitivity likely make any such comparison fraught with systematics. We find BLA frequencies of $dn(\text{BLA})/dz = 16$ and 12 using $S/N = 20$ and 10, respectively, for $N(\text{H I}) \geq 10^{13.2} \text{ cm}^{-2}$ in the d32n256vzw150-bturb simulation, compared to 30 ± 4 from Lehner et al. (2007). However, 39% of these absorbers have $N(\text{H I}) > 10^{14.0} \text{ cm}^{-2}$, while the data shows a lower fraction of strong BLAs. We appear to be missing a population of weak BLAs; however we leave a detailed comparison of such properties for future work during the COS era.

Our review of H I finds we reproduce most key observables; only subtle disagreements among our various models are noticeable, and then only for strong lines above $N(\text{H I}) = 10^{14} \text{ cm}^{-2}$. These disagreements may be related to (1) detailed differences between processing observed and simulated spectra, and (2) the inability of simulations to resolve absorbing substructures in halo gas. The strongest winds make 20% fewer $N(\text{H I}) = 10^{14.0-17.0} \text{ cm}^{-2}$ absorbers at all redshifts below $z = 1$, while added turbulence appreciably broadens only absorbers with $N(\text{H I}) \geq 10^{14.0} \text{ cm}^{-2}$. Much remains to be learned about the observed low- z Ly α forest by comparing simulations to future observations with COS, especially for BLAs; we leave for future work examining the entire Lyman series with identical reduction and analysis methods applied to observed and simulated spectra.

3.2 O VI Observables

We now consider three robust O VI observables with trends corroborated by multiple groups. We explain their physical significance, and then explore how each of our models, all at the same resolution, fits these three sets of data. Lastly, we compare models at different resolutions to examine the issue of numerical resolution convergence.

The cumulative $EW(\text{O VI})$ component distribution (1032 Å line) below $z \leq 0.5$, shown in the left panels of Figure 4, is the most commonly published low- z O VI observable. It is relatively independent of spectral resolution and noise, so long as a given equivalent width systems is

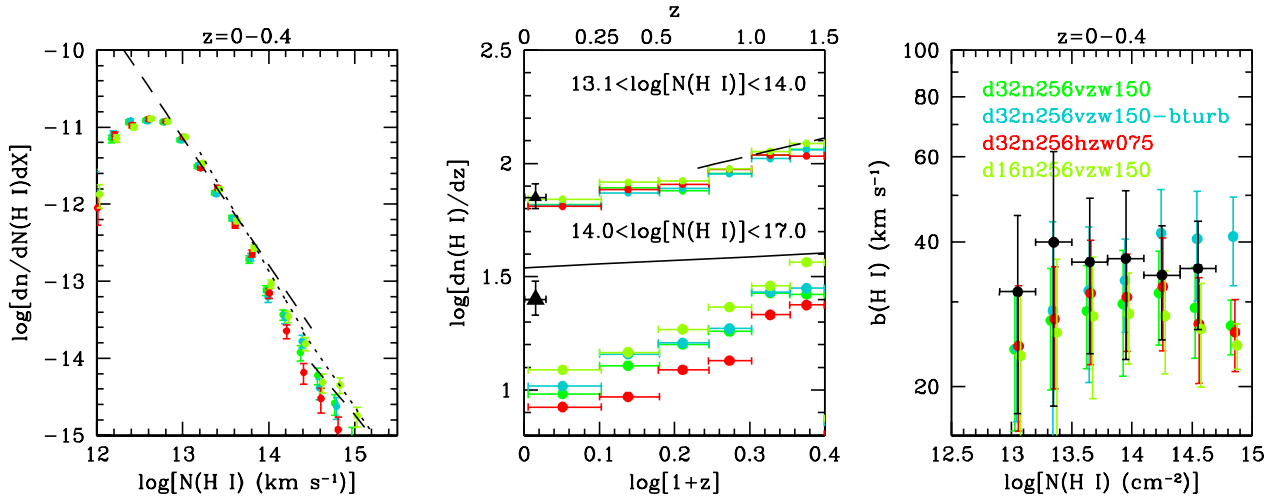


Figure 3. Four of our models, d32n256vzw150 with and without sub-SPH turbulence added, d32n256hzw075, and d16n256vzw150, are shown against three general H I observables. The left panel shows our differential column density distribution compared to the power law fits to data of Lehner et al. (2007, dotted line, $b < 40 \text{ km s}^{-1}$ only) and Penton et al. (2004, dashed line). In the central panel, the evolution below $z = 1.5$ in two bins ($N(\text{H I}) = 10^{13.1-14.0}$ & $10^{14.0-17.0}$) is plotted relative to Weymann et al. (1998, solid line), Janknecht et al. (2006, long dashed line), and Penton et al. (2004, triangles with large/small symbols corresponding to the strong/intermediate bin). Line width as a function of $N(\text{H I})$ in our simulations is shown in the right panel compared to Lehner et al. (2007) with one extra bin considered for our larger simulated sample. We fit $\text{Ly}\alpha$ for $N(\text{H I}) \leq 10^{14.4}$ and $\text{Ly}\beta$ for higher column densities when considering b -parameters. Turbulence broadens the stronger H I lines noticeably.

identifiable. T08 performed a blind O VI search (i.e. search for the O VI doublet alone without requiring corresponding H I), explicitly differentiating between components and systems. DS08 identify O VI associated with H I absorbers, and estimate they miss $\sim 20\%$ of O VI absorbers this way. Their larger sample has the advantage of reaching down to 10 mÅ . This is especially important, because Tumlinson & Fang (2005) suggest that a turnover in this distribution indicates the extent to which metals are distributed to lower overdensities. The turnover in the DS08 data set is not as pronounced as in the smaller Danforth & Shull (2005) dataset at 30 mÅ . We will argue that the declining numbers are weakly indicative of a metallicity gradient with density. Figure 1 illustrates the decline in O VI at weak column densities; fewer regions exist where $N(\text{O VI}) \lesssim 10^{13} \text{ cm}^{-2}$ (green regions in the bottom right) compared to H I (bottom left), which is not observed to turnover at $N(\text{H I}) \lesssim 10^{13} \text{ cm}^{-2}$ (e.g. Penton et al. 2004).

Our second observable is $b(\text{O VI})$ as a function of $N(\text{O VI})$. In the literature, this plot is often used to diagnose the physical state of absorbers, as in Heckman et al. (2002). That paper models O VI absorbers as radiatively cooling flows passing through the coronal temperature regime, finding a linear correlation between $N(\text{O VI})$ and $b(\text{O VI})$ corresponding to the cooling flow velocity, and independent of density and metallicity. They also show non-IGM O VI absorbers (O VI around local group galaxies and starbursts) follow this relation very closely, and Lehner et al. (2006) finds that IGM absorbers agree with the same trend. However, this latter paper fails to match the predicted $N(\text{Ne VIII})/N(\text{O VI})$ ratios, and suggests the IGM lines may instead be photo-ionized. Danforth et al. (2006) also do not see O VI absorbers following the Heckman et al. (2002) trend, but note that their lines may suffer from blending and exaggerated b -parameters.

We use only the highest resolution (STIS) data of intervening absorbers from T08, and plot these 55 absorbers spanning $z = 0.13 - 0.50$ in 0.2 dex bins in the central panels of Figure 4, with 1σ dispersions. We consider $b(\text{O VI})$ as a function of $N(\text{O VI})$ (rather than vice-versa) because we will show that our absorbers are primarily photo-ionized with the underlying relation being density- $N(\text{O VI})$. A clear upward trend is obvious in this data sample with lines $N(\text{O VI}) > 10^{14} \text{ cm}^{-2}$ averaging 35.6 km s^{-1} . These lines cannot be explained by thermal broadening alone, because the thermal b -parameter is only 17.7 km s^{-1} for the optimal O VI CIE temperature of $\approx 300,000 \text{ K}$. Hence there is extra broadening in these lines; possibilities include instrumental broadening, Hubble flow broadening, and turbulent broadening, all of which we will explore.

The final observable is $N(\text{O VI})$ as a function of $N(\text{H I})$ for well-aligned components, shown in the right panels of Figure 4. Danforth & Shull (2005) fit this relation with a $N(\text{H I})^{0.1}$ power law, i.e. $N(\text{O VI})$ rises very mildly with $N(\text{H I})$. They thus argue that these two ions trace different IGM phases, with O VI tracing collisionally ionized gas, and consider this the multi-phase ratio. T08 also finds very little variation of $N(\text{O VI})$ with $N(\text{H I})$, but show that single-phase photo-ionized models can reproduce much of this trend if metallicities are allowed to vary. They find their aligned absorbers are well-described by the median of their robust O VI sample, $N(\text{O VI}) = 10^{13.84} \text{ cm}^{-2}$, shown as a solid line. They further argue that well-aligned O VI with H I is most likely photo-ionized; this conclusion is also reached by Thom & Chen (2008a), who argue that slightly increasing O VI strength with greater $N(\text{H I})$ implies a declining ionization parameter with increasing gas column density. The specifics of the physics revealed by this trend are explored further in §4.3.1.

We define “well-aligned” O VI and H I absorption as hav-

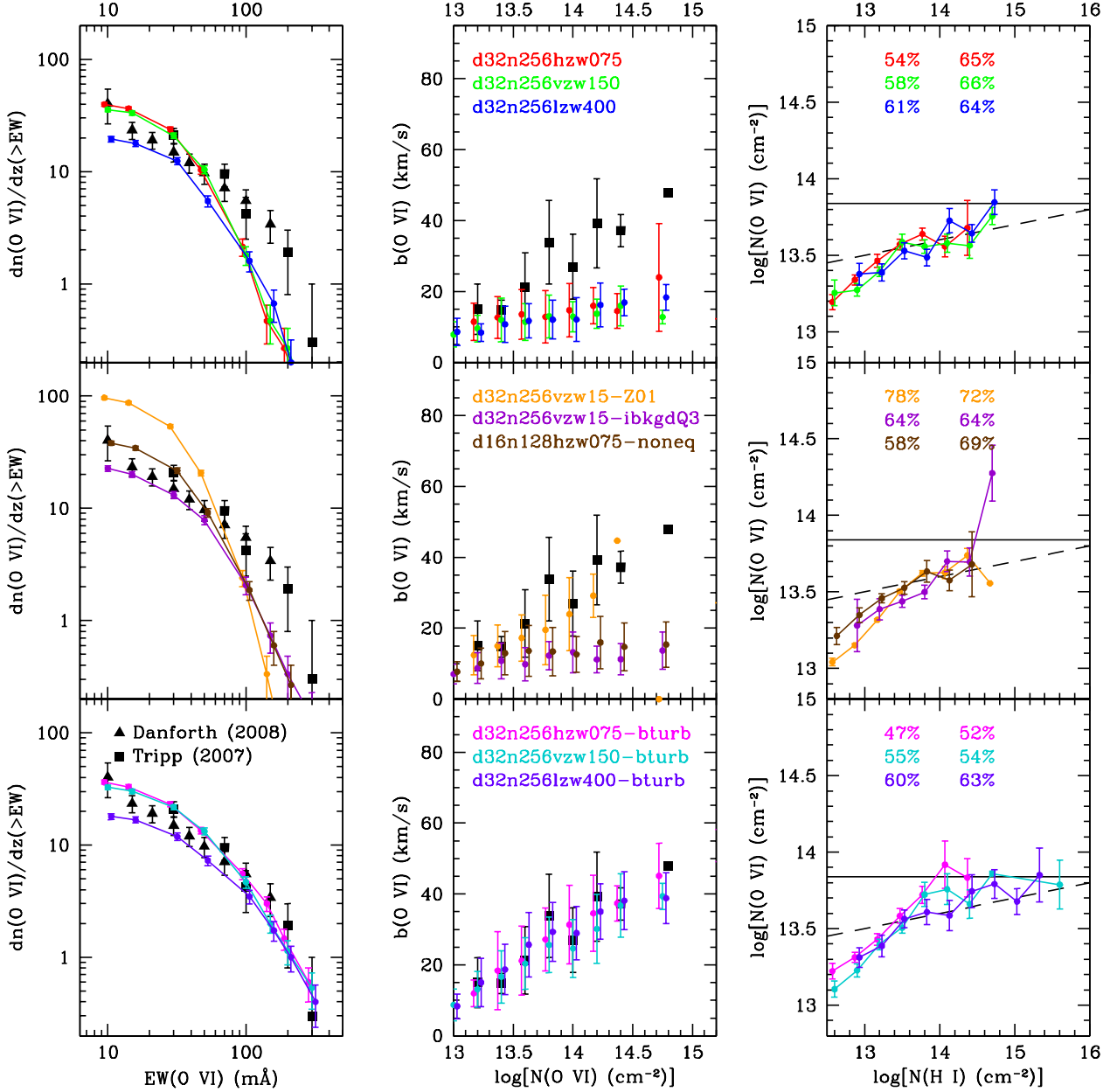


Figure 4. Nine models are fit to three O VI observables: the cumulative EW distribution (left) with data from T08 (squares) and DS08 (triangles), $b(O\text{ VI})$ as a function of $N(O\text{ VI})$ (center) over $z = 0.15 - 0.5$ from T08 components, and the $N(O\text{ VI})$ as a function of $N(\text{H I})$ (right) with a fit from Danforth & Shull (2005) (dashed line) and the relation from T08 (where $N(O\text{ VI}) = 10^{13.84} \text{ cm}^{-2}$, solid line) along with two percentages indicating the fraction of well-aligned O VI absorbers with $N(O\text{ VI}) = 10^{13.5-14.0}$ (left) and $N(O\text{ VI}) = 10^{14.0-15.0}$ (right); the corresponding observed alignment fractions are 57 and 43% respectively. The top panels explore how different wind models fit. The middle panels explore other model variations such as a quasar-only ionization background scaled to the H I ionization rate, a uniform $Z = 0.1 Z_{\odot}$ metallicity distribution, and non-equilibrium ionization ratios from Gnat & Sternberg (2007) for O VI at CIE densities. The bottom panels show the addition of sub-SPH turbulence for all three wind models, which we suggest are small-scale velocities below our resolution limit in our simulations, yet provides the best fit to the data by broadening lines and increasing the EW of the strongest absorbers. Error bars show 1σ errors in the left and right panels, while in the center panel they indicate 1σ dispersions to indicate the range of b -parameters. Slight offsets in the x-axis values are for the ease of visibility.

ing $\delta v \equiv |v(\text{H I}) - v(\text{O VI})| \leq 8 \text{ km s}^{-1}$, which corresponds to a Hubble-broadened spatial extent of $103 \pm 3 \text{ kpc}$ given the uncertainty in cosmological parameters from the WMAP5 results. We compare our models to the T08 dataset by applying the exact same criteria in searching for the closest H I component to every O VI component. We only consider absorbers at $N(O\text{ VI}) \geq 10^{13.5} \text{ cm}^{-2}$, which is essentially a

complete sample in $S/N \geq 10$ spectra. For the same reason, we require $N(\text{H I}) \geq 10^{12.9}$, so that an observed high- S/N sight line does not have a greater alignment fraction due to more detected weak H I absorbers compared to a low- S/N sight line. A single H I component is allowed to be associated with multiple O VI absorbers; the converse is *not* applicable when we discuss the fraction of H I absorbers aligned with

O VI later in 5.2. T08 applies an alignment criteria that considers instrumental resolution (see their §2.3.3), but we use a simple limit of 8 km s^{-1} because almost every component is determined to an error below this limit. We use the T08 dataset over the Thom & Chen (2008a) dataset because the former is larger and spans a larger range of $N(\text{O VI})$. We make an exception for one strong system at $z = 0.20266$ in PKS 0312-770, since T08 does not fit H I owing due to large uncertainties, and we instead use the parameters found by Thom & Chen (2008b). This is an important system, because it is one of the strongest O VI absorbers with the strongest aligned H I.

In the upper left area of the right-hand panels in Figure 4 we show two percentages, corresponding to the fraction of well-aligned O VI components in two intermediate-strength $N(\text{O VI})$ bins: $10^{13.5-14.0}$ and $10^{14.0-15.0} \text{ cm}^{-2}$. For comparison, the T08 dataset has 57% and 43% of strong absorbers well-aligned in the low and high bins respectively by our criteria. T08 considers 37% of their O VI *systems* aligned, however this is a very different consideration where such systems have a single O VI component well-aligned with H I. We do not consider simple versus complex systems as defined by T08, because the definitions are not easily applicable to an automated procedure as we run on our simulations; comparing simulated and real systems is a challenge left for a future paper where the data reduction and analysis are replicated as closely as possible.

In the following subsections, we step through each of our models, and assess how the variations in input physics impact observable properties. We emphasize the observables that differentiate amongst models in the discussion below. We save the interpretation of well-aligned absorbers for a detailed examination of ionization models in §4.3.1

3.2.1 Wind Velocity Strength

The top panels of Figure 4 show a comparison between our three wind models, with our default `specexbin` parameters. For all three wind models, there is a clear dearth of high-*EW* lines, and the observed line widths are progressively larger than predicted to higher $N(\text{O VI})$. Hence wind strength does not affect the high-*EW* components nor their *b*-parameters, which is an indication that the strongest lines are saturated and depend little on their actual metallicity as long as it is above a certain threshold. Since varying wind strength cannot explain these data, we require another explanation, which we will explore in the coming sections. Cen & Fang (2006) also find their simulations with and without superwinds make no difference at $EW \geq 100 \text{ mÅ}$; however our SPH code versus their grid-based code treats the distribution of metals on large scales very differently. In our case, GADGET-2 simulations without outflows barely produce any IGM absorbers (Springel & Hernquist 2003; OD06), thus we do not explore this case at low- z .

Varying the strength of the winds has the largest observable consequence for the number of low-*EW* O VI components. Comparing *vzw* and *lzw* best illustrates the suggestion of Tumlinson & Fang (2005) that the turnover seen at low *EW* is a consequence of declining IGM enrichment further from galaxies, and can be used to constrain the extent of the dispersal of metals. Fang & Bryan (2001) find their simulations generate a turnover in the *EW* distribu-

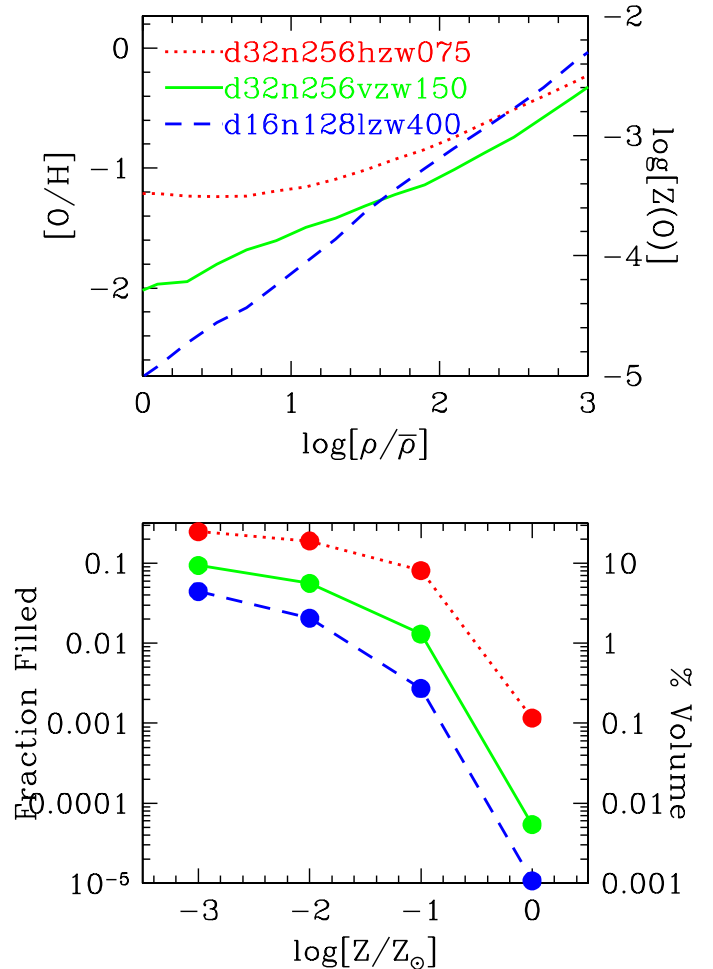


Figure 5. The average metallicity per density for the three wind models in the top panel show that while all wind strengths form a metallicity-density gradient, stronger winds flatten this relationship. The volume filling factors at various limiting metallicities in the bottom panel indicate wind strength plays a major role. At $Z = 0.1 Z_{\odot}$, a factor of 27 reduction in volume filling factor across the three wind models is reflected in observations only by 50% fewer weak components.

tion at $z = 0$ due to a metallicity-density gradient. Indeed, all our simulations produce metallicity-density gradient as we display in the top panel of Figure 5; OD06 also showed strong gradients at higher redshift. While the steeper gradient of the *lzw* model yields an observational signature, the milder flattening of the *hzw* below overdensities of 10 has no observable effect.

O VI does not distinguish the density-metallicity gradient well; however, a key point is that our O VI absorbers arise from a fairly small volume filling factor of metals, and this is strongly governed by v_{wind} . By $z = 0.25$, our three simulations have volume filling factors where $Z \geq 0.01 Z_{\odot}$ (determined from oxygen) of 1.9%, 5.5%, and 18.0% as v_{wind} increases (*lzw* \rightarrow *vzw* \rightarrow *hzw*). We determine these filling factors from lines of sight in physical space (i.e. no velocity smearing) using `specexbin`, plotting them in the bottom panel of Figure 5 for various metallicities. O VI generally arises from regions with $Z \geq 0.1 Z_{\odot}$, where volume filling factors are only 0.3%, 1.3%, and 8.1% with increasing v_{wind} . The *lzw*

model differentiates between the amount of volume filled with half as many absorbers at $EW = 15 \text{ m\AA}$ and below, but the vzw and hzw models are indistinguishable despite even larger disparities in the volume filled. This disparity grows even further at the Z_{\odot} limit; the hzw model enriches $18\times$ more volume than the vzw model, which fills only $1/15,000$ th of a cosmological volume! These relatively small filling factors in our simulations are a consequence of the fact that, as we showed in Davé & Oppenheimer (2007) and OD08, winds at late times enrich an increasingly smaller comoving volume, while many of the metals launched at early times reaccrete onto galaxies. Hence metals increasingly reside in compact high-overdensity regions at lower redshifts.

It is remarkable that an order of magnitude change in the volume filling factor at the fiducial O VI metallicity is observationally indistinguishable. It is not mysterious however, because the mass-weighted oxygen abundance (only 7% less in vzw compared to hzw) determines most trends in the observables. The Figure 1 slice of the d32n256vzw150 simulation illustrates that the volume enriched (upper right) does not correlate to where observable O VI is (bottom right; compare blue, pink, & white regions).

The alignment of H I and O VI appears to provide no indication of the metallicity distribution either. The percentage of aligned components is statistically indistinguishable in the two $N(\text{O VI})$ bins in the upper right panel of Figure 4 as well, which could be considered surprising given how differently oxygen is distributed. We take this as an indication that the peculiar velocities are more important when considering aligned components rather than spatial distribution. It is disappointing that one cannot constrain the metallicity-density gradient or the volume filling factor from $EW(\text{O VI})$, despite O VI being an ideal tracer of photo-ionized low-density metals (Davé et al. 1998).

3.2.2 Uniform $Z = 0.1 Z_{\odot}$ Distribution

In the middle row panels of Figure 4 we explore variations of post-run physics. Applying a uniform metal distribution (orange lines in the middle panels) goes in the opposite direction of how our models need to be modified to fit the EW distribution, since there are now more metals in low-density regions and fewer in high-density regions compared to our self-consistent enrichment models, which have metallicity-density gradients shown in Figure 5. Conversely, it illustrates the possibility of explaining large b -parameters with spatially extended structures undergoing Hubble expansion. Stronger components do show greater spatial broadening, with $b \sim 30 \text{ km s}^{-1}$ at $N(\text{O VI}) \geq 10^{14.1} \text{ cm}^{-2}$ corresponding to spatial scales of $\sim 400 \text{ kpc}$. With 100% volume filling factor of $Z \geq 0.1 Z_{\odot}$, the number of $\geq 10 \text{ m\AA}$ components only triples over the d32n256vzw150 wind-distributed metals, which has a volume filling factor $80\times$ less; again, this shows that low- EW lines are a weak tracer of volume filling factor. Lines with $EW \geq 100 \text{ m\AA}$ are statistically indistinguishable suggesting that these thin lines are already saturated with only $0.1 Z_{\odot}$.

The slope of $N(\text{H I}) - N(\text{O VI})$ relation steepens due to more weak O VI absorbers, because there is an excess of such components near the O VI detection limit. This model does show a 17% higher incidence of well-aligned components with $N(\text{O VI}) = 10^{13.5-14.0} \text{ cm}^{-2}$ (78%) than any other

model, which is a statistically meaningful difference. Metals are smoothly distributed over the same fluctuations that create H I absorption leading to this higher fraction. The fact that the T08 dataset finds a lower fraction (57%) is an indication that metals are distributed differently than baryons traced by H I. In summary, applying a uniform metallicity does not appear to reconcile the models and observations.

3.2.3 Ionization Background

The middle row of Figure 4 illustrates the impact of varying the ionizing background. 37% fewer $EW \leq 30 \text{ m\AA}$ O VI lines create a more obvious turnover when the quasar-only background is tripled (*ibkgd-Q3*), while leaving the Ly α forest statistics nearly unchanged. The peak of photo-ionized O VI ionization fractions moves to higher overdensities due to the higher ionization parameter at 8.4 Rydbergs, resulting in O VI not tracing lower overdensities (~ 10) nearly as much, and leading to an underestimate of weak absorbers relative to the data. If future datasets from COS show a greater downturn in the EW distribution, then perhaps this harder ionization field is more appropriate. Little is known about the ionization field at 8.4 Rydbergs, however the quasar+galaxy Haardt & Madau (2001) background works extremely well for both the H I and O VI observables we consider.

The *ibkgd-Q1* background leaves the O VI statistics unaltered, but creates significantly more H I absorption, in conflict with observations. We do not plot this in Figure 4 as the only change is the H I – O VI relation moves rightward by nearly 0.5 dex due to greater H I optical depths at a given overdensity.

3.2.4 Non-Equilibrium Ionization

Lastly, the middle row panels of Figure 4 illustrate the impact of non-equilibrium cooling. Gnat & Sternberg (2007) calculate non-equilibrium ionization states and cooling efficiencies for rapidly cooling shock-heated gas without any ionization background. Since recombination lags cooling, the temperature range over which collisionally ionized O VI can exist extends below $T = 10^5 \text{ K}$. When we apply only their metallicity-dependent ionization fractions (their isochroic case) to where O VI is primarily collisionally ionized (i.e. $n_h > 10^{-4.1} \text{ cm}^{-3}$ at $z = 0.25$), we find a slight but immeasurable increase in O VI absorption from complex systems tracing halo gas. Collisionally ionized O VI is primarily found near galactic halos, which have a small volume filling factor at low- z (see §5.3).

Cen & Fang (2006) added non-equilibrium ionization directly to their simulations, and find an appreciable reduction in O VI tracing lower overdensities, because it is here that CIE timescales are longer than shock-heating timescales; O VI remains in CIE longer in the equilibrium case. Similar two-temperature behavior was shown by Yoshida et al. (2005) to have observational consequences in WHIM and ICM gas when applied to their cosmological simulations. Hence it is possible that including non-equilibrium ionization self-consistently during the simulation may yield a larger difference.

As an initial attempt towards this, we run the d16n128hzw075-noneq simulation with non-equilibrium

metal-line cooling from Gnat & Sternberg (2007) *during* the run. However, this creates no appreciable difference in O VI either. The broader metal-line cooling bumps actually appear to make it slightly easier for baryons to cool into galaxies, and there is a slight increase in Ω_*/Ω_b at $z = 0$ (6.3% versus 5.7% from our d16n128hzw075 test simulation). However, O VI observables are insensitive to such a small change in star formation, and the brown curves in the middle row panels of Figure 4 are indistinguishable from the assumption of CIE.

Density-dependent non-equilibrium ionization effects with the inclusion of an ionization background could affect photo-ionized O VI, especially given the fact that these metals get into the diffuse IGM via shocked outflows. Recombination timescales exceed the Hubble time in such regions, and the two-temperature behavior of ions and electrons may have unforeseen consequences, possibly moving oxygen seen as O VI to higher ionization states. It remains to be seen how big of an effect this is, and non-equilibrium effects on photo-ionized O VI will be necessary to explore.

Overall, non-equilibrium ionization effects may have some impact on weak O VI systems, but is unlikely to provide an appreciable change to b -parameters as required to match the $N(\text{O VI}) - b(\text{O VI})$ relation. We plan to implement full non-equilibrium oxygen network during our simulation run to study this possibility further, but it seems unlikely to yield a large difference.

3.2.5 Sub-SPH Turbulence

We now consider the by-hand addition of sub-resolution turbulence, given by b_{turb} as described in Equations 5 and 6. In this case, T08’s observed $N(\text{O VI}) - b(\text{O VI})$ relation in the bottom center panel of Figure 4 is reproduced by construction. However, an added consequence of the broader lines is that some of the lines that were saturated in the non-turbulent case now lie on the extended linear portion of the curve of growth. Their equivalent widths grow dramatically, and these models provide a good fit to the cumulative EW distribution at 50 mÅ and above. Our favored model, the d32n256vzw150-bturb, matches the T08 EW distribution as well as the 10 mÅ data of DS08. All the wind models shown in the bottom panels behave in the same way relative to each other as discussed in §3.2.1.

A major caveat is that, as we show in §3.2.6, the overall abundance of O VI absorbers is not completely converged with numerical resolution, in the sense that higher resolution runs tend to show more absorbers at high EW . Hence the good agreement with d32n256vzw150-bturb should be taken with some caution, and our wind model may need further refinement. The robust result here is that only the addition of turbulence is able to change the *shape* of the EW distribution to resemble that observed.

We focus on the differences between turbulent and non-turbulent cases in Figure 6, where we have included the d32n256vzw150 and d32n256vzw150-bturb models along with the higher resolution d16n256vzw150 model, which we discuss below. Turbulence blends components, primarily weaker ones in complex systems, which would be identified individually without turbulence; this is evidenced by 21%

fewer 10-30 mÅ components¹, and could be only a minor factor in explaining the turnover at low- EW . When considering $\Omega(\text{O VI})$ by summing all components between $10^{12.5} - 10^{15.0}$ using equation 6 of DS08, we find $\Omega(\text{O VI}) = 3.8 \times 10^{-7}$ with turbulence², only 5% more than without; turbulence should not affect column densities much, because the same amount of O VI remains in a sight line.

Both simulations have the same amount of O VI along a line of sight, but AutoVP will often fit components with and without turbulence dramatically differently. An example is an absorber at $z = 0.19$ where the turbulently broadened line is fitted with $N(\text{O VI}) = 10^{14.73} \text{ cm}^{-2}$, $b = 38 \text{ km s}^{-1}$, and $EW = 305 \text{ mÅ}$, versus $N(\text{O VI}) = 10^{14.33} \text{ cm}^{-2}$, $b = 9.4 \text{ km s}^{-1}$, and $EW = 90 \text{ mÅ}$ in the non-turbulent case. Without turbulence, much of the O VI remains hidden in the saturated line center. T08 finds no lines with at least $10^{14.3} \text{ cm}^{-2}$ having b -parameters under 33 km s^{-1} using STIS. This is the typical absorber that greatly enhances the high end of the turbulent EW distribution, increasing it by $2.8\times$ despite having the same underlying physical distribution of O VI along the sight line.

Every single one of our models follows shows increasing $N(\text{O VI})$ with $N(\text{H I})$, which as Thom & Chen (2008a) argue indicates a decreasing ionization parameter for stronger O VI, and suggests a photo-ionized origin. The aligned absorber percentages in the lower bin are only 2% apart with and without turbulence, and agree statistically with the T08 percentages. There are more aligned absorbers at $N(\text{H I}) > 10^{14.5} \text{ cm}^{-2}$, because of the blending of separate H I components in very dense regions due to added turbulence.

It is worthwhile to ask whether it is fair to add such a “fudge factor” in our models just to fit the data. In its favor, it does separately alter the shape of the EW distribution as desired, and there seem to be no other effects capable of doing so. Still, it is an unsatisfyingly ad hoc addition, and in §4.4 we attempt to further explore the physics responsible for b_{turb} , and understand their implications for small-scale motions in the IGM.

3.2.6 Resolution Convergence

We use the d16n256vzw150 simulation only to test resolution convergence, and not to explore the general properties of O VI absorbers, since it does not contain a statistical sample of galaxies at M^* nor a representative volume of low- z environments. Although the d16n256vzw150 simulation produces 40% more star formation, this is not evidenced in the low end of the EW distribution in Figure 6 where there exist 26% *fewer* absorbers between 10-50 mÅ than the d32n256vzw150 simulation. The excessive late-time star formation in the d16n256vzw150 simulation (as mentioned in §2.1) enriches mainly higher overdensities probed by stronger O VI absorbers (50% more 100 mÅ O VI

¹ The cumulative EW distribution only shows a 7% difference summing all absorbers $\geq 10 \text{ mÅ}$.

² This value compares favorably with DS08’s value of $4.1 \pm 0.5 \times 10^{-7}$ above a similar limit (30 mÅ), but we do not wish to draw too much into this comparison, since our simulation resolution limits may be hiding more O VI, see §3.2.6.

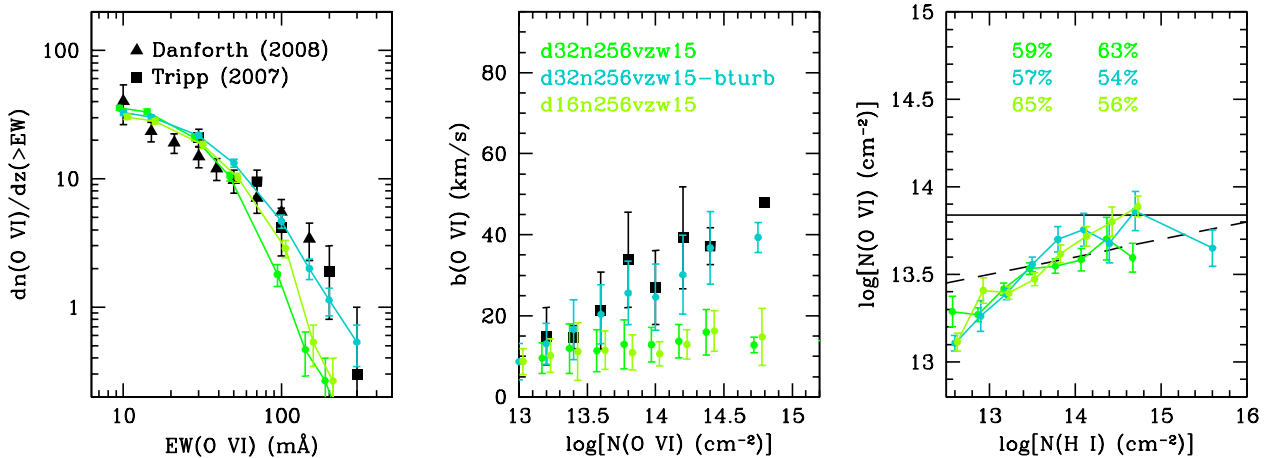


Figure 6. Three models with *vzw* winds are plotted against the same three O VI observables in Figure 4. The d32n256vzw150 and d32n256vzw150-bturb are plotted on the same panels to directly show how turbulence affects observational signatures, while the d16n256vzw150 model explores the effect of increasing mass resolution by $8\times$.

absorbers) and lower ionization metal species. Although the d16n256vzw150 simulation is resolving more galaxies down to $\sim 10^8 M_\odot$, these galaxies do not seem to be a significant contributor to the IGM O VI. Instead, the difference for low-*EW* absorbers appears to depend on the hydrodynamics of outflows at different resolutions—winds from the same mass galaxy at higher resolution do not enrich as effectively low density regions where weak O VI absorbers arise. This could be a result of more resolved substructure leading to greater hydrodynamic slowing at higher resolutions. We caution that the differences could also be partly numerical artifacts inherent to SPH, such as excessive viscosity and poor two-phase medium separation. Furthermore, there is no evidence we can resolve the sub-SPH turbulence any better at $\times 8$ greater resolution as evidenced by the *b*-parameters showing nearly no change between the two simulations; this turbulence must be added explicitly at cosmological resolutions.

The $N(\text{H I})/N(\text{O VI})$ ratio in right panel of Figure 6 again shows essentially no difference between the two resolutions. There are more strong aligned O VI absorbers above $N(\text{O VI}) = 10^{14.1} \text{ cm}^{-2}$ due to greater enrichment of overdense regions in the d16n256vzw150 box.

We do not explore our d64n256vzw150 box, because (1) this simulation significantly underestimates SF at $z > 2$ as it cannot resolve below M^* at these redshift, and (2) the mean interparticle spacing is greater than the sizes of absorbers ($50 - 100 \text{ kpc}$) we find in the next section. The $32h^{-1} \text{ Mpc}$ 256^3 is above the critical resolution where we can resolve the production of metals in O VI absorbers and the sizes we derive for these absorbers.

Overall the resolution convergence of O VI absorber properties, while mostly statistically consistent in Figure 6, indicate some numerical issues within our simulations. It appears unlikely that modest increases in resolution will dramatically change the basic conclusion that sub-SPH turbulence is needed to match O VI observations. Running simulations with sufficient resolution to study small-scale turbulence while properly modeling nonlinear structures to $z = 0$ is well beyond present computing abilities. We further stress the need to run galactic-scale simulations in the future to

fully resolve the absorbing structures within haloes and intragroup gas where the strongest O VI absorbers appear arise in our simulations.

Finally, concerning box size convergence, it is true that the $32h^{-1} \text{ Mpc}$ does not contain larger modes that could become non-linear by $z = 0$; however we will show that we are primarily exploring the diffuse IGM around sub- M^* galaxies, which are statistically well-sampled in our simulation. This is evidenced by the fact that our O VI and H I statistics in the d16n128vzw150 box are statistically consistent with those of the d32n256vzw150 box.

4 PHYSICAL CONDITIONS OF O VI ABSORBERS

From here on we focus on our favored model with sub-resolution turbulence added, d32n256vzw150-bturb, and examine the physical nature of O VI absorbers. We first examine the density, temperature, metallicity, and absorber size of IGM O VI components, finding that most observed O VI systems are consistent with being photo-ionized. Shorter cooling times of a clumpy metal distribution are argued as the driver for O VI to reach such temperatures. We then discuss the correspondence of H I with O VI, using the $N(\text{H I}) - N(\text{O VI})$ relation to explore various photo-ionization, collisional ionization, and multi-phase ionization models. Lastly, we justify adding turbulent velocities on physical grounds, explaining why it should not be surprising that turbulence provides a dominant component to many IGM absorber profiles. This will lead us to the next section where we examine the location and origin of O VI relative to galaxies.

Physical parameters ascribed to absorbers such as density and temperature can be weighted in multiple ways. Possibilities include H I and O VI absorption weighting, or just normal mass weighting. We weight such quantities using the formula

$$X(W) = \frac{\sum W \times X}{\sum W} \quad (7)$$

where X is the property and W is the weight. For exam-

ple, if a quantity is weighted by O VI absorption, $W = m \times Z_{\text{O}} \times f(\text{O VI})$, where m is mass of the element (e.g. SPH particle), Z_{O} is the mass fraction in oxygen, and $f(\text{O VI}) \equiv \text{O VI}/\text{O}$ (the O VI ionization fraction). X is often temperature or density itself. The difference between H I and O VI-weighted quantities is critical for understanding the multi-phase nature of absorbers.

We examine 70 continuous lines of sight with $S/N = 20$ between $z = 0.5 \rightarrow 0$; we call this is our high quality sample. 1511 O VI components are identified above $N(\text{O VI}) = 10^{12.5} \text{ cm}^{-2}$. This sample allows us to obtain reasonable statistics of all absorbers between $N(\text{O VI}) = 10^{12.9-14.9} \text{ cm}^{-2}$, which we will refer to as the “observed range” since nearly all observed IGM O VI absorbers lie in this interval.

4.1 A photo-ionized model for O VI absorbers

We examine the density, temperature, metallicity, and sizes of O VI absorbers based on the observational quantity $N(\text{O VI})$. Figure 7 (top two panels) plots the median O VI-weighted density and temperatures at the line centers. Over two decades of column density covering the observed range, O VI absorbers show a steady increase in n_{H} , while the temperature stays nearly constant at $T \sim 10^{4.15} \text{ K}$. Also plotted in dashed lines are the 16th and 84th percentile values corresponding to the 1σ dispersions. The scatter in density is significantly larger, $\sigma = 0.3 - 0.4 \text{ dex}$, compared to the scatter in temperature, $\lesssim 0.2 \text{ dex}$ over much of the observed range. Our first main conclusion is that the vast majority of O VI absorbers at all but the very strongest column densities are photo-ionized, with temperatures less than 30,000 K.

We already presented the fit to the density as a function of $N(\text{O VI})$ in Equation 4, which fits the relation quite well regardless of added turbulence (magenta dashed line). The increase in density alone can explain 66% of the O VI column density increase, with all else being equal. The remaining increase must arise from variations in metallicity, ionization fraction, and absorber length. Metallicity is expected to explain some of the increase, because our simulations show a consistent metallicity-density gradient, as shown in Figure 5. Fitting the points in the third panel of Figure 7 yields the relation

$$\log[Z_{\text{O}}] = 0.45 \times \log[N(\text{O VI})] - 8.96, \quad (8)$$

for $N(\text{O VI}) = 10^{12.9-14.9} \text{ cm}^{-2}$. Although density (66%) and metallicity (45%) variations can account for all of the dependence of $N(\text{O VI})$, we will show that ionization fraction and absorber length also vary.

The metallicities reported here always exceed the fiducial value of $0.1 Z_{\odot}$ often assumed when modeling low- z O VI absorbers. Our absorbers are generally found to lie between $0.15-1.0 Z_{\odot}$, which is consistent with metallicity determinations from aligned H I absorbers (Prochaska et al. 2004; Lehner et al. 2006; Cooksey et al. 2008, ; T08). We contrast the oxygen-weighted metallicity of O VI absorbers (Equation 8) to the mass-weighted oxygen metallicity-density gradient averaged over the entire simulation box at $z = 0.25$:

$$\log[\bar{Z}_{\text{O}}] = -4.26 + 0.36 \log[\rho/\bar{\rho}] + 0.075 (\log[\rho/\bar{\rho}])^2, \quad (9)$$

for $\rho/\bar{\rho} = 1 - 3000$, which is a fit to the green curve in the top panel of Figure 5. This shows a 34% rise over the same

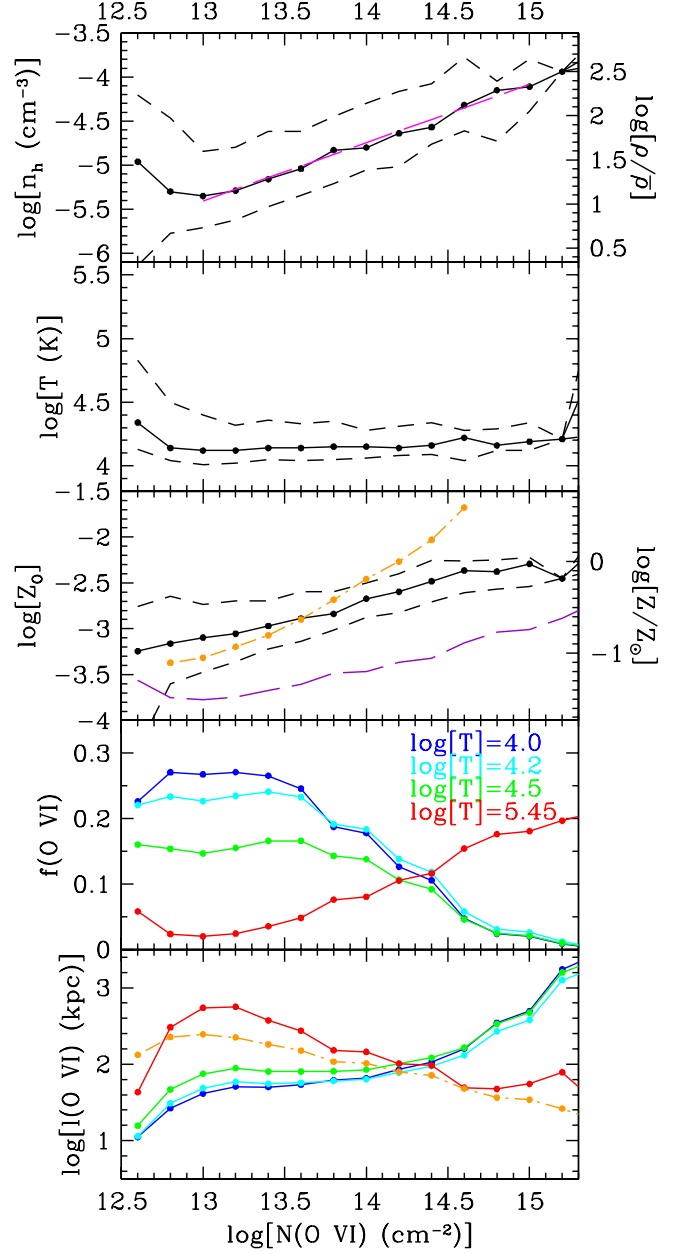


Figure 7. Physical properties as functions of O VI column density in the d32n256vzw150-bturb model are plotted a solid black lines with points in the top 3 panels for all our simulated absorbers in 70 high-quality lines of sight below $z = 0.5$. Dashed lines correspond to 1σ dispersions. The long-dashed magenta line is the fit from Equation 4. We also plot the simulations-average metallicity as a function density (converted to $N(\text{O VI})$ via Equation 4, purple long-dashed line) and the metallicity one would infer using aligned $N(\text{H I}) - N(\text{O VI})$ absorbers as in Equation 15 (orange dashed-dot line). We consider O VI fractions from CLOUDY at three photo-ionized temperatures (2nd to last panel), which suggest photo-ionized O VI absorbers are typically 50-100 kpc long (last panel). O VI in CIE will produce more compact absorbers at higher $N(\text{O VI})$ (red lines), which appear to trace gas near and within halos. The H I-derived absorber length (orange dashed-dot line) assuming O VI traces the same gas as H I appears to be a poor approximation for strong absorbers, suggesting such aligned absorbers are multi-density.

$N(\text{O VI})$ range, and is represented by the purple dashed line in the middle panel of Figure 7. The metallicities of O VI absorbers are on average $4 - 6\times$ higher than the general IGM over the observed range. This is a clear sign that O VI absorbers trace inhomogeneously distributed metals. The low scatter in the oxygen metallicity-density relation indicates that O VI absorbers rarely trace gas with average IGM metallicity. Hence the global metallicity-density relationship is a poor descriptor of the enrichment level in metal-line absorption systems.

The fourth panel in Figure 7 shows the O VI ionization fraction, computed by assuming the density- $N(\text{O VI})$ relation shown in the top two panels, for various temperatures, assuming a Haardt & Madau (2001) quasar-only background. For a typical O VI temperature of $T = 10^{4.2}$ K, $f(\text{O VI})$ changes significantly from 0.23 to 0.029 over the observed range. It depends little on temperature for lines above 10^{14} cm^{-2} . The peak ionization fraction for collisional ionization ($T = 10^{5.45}$) is around 0.2, but it is only approached for the strongest lines. This is another reason why over most of the observed range, photo-ionization is the dominant mechanism for O VI absorbers.

Thus far, the dependence of $N(\text{O VI})$ using photo-ionization is partially explained by density (66%) and metallicity (45%), but the declining ionization fractions above $n_{\text{H}} = 10^{-5.0} \text{ cm}^{-3}$ anti-correlate with $N(\text{O VI})$ (-45%). The remaining dependence (34%) therefore must be in the absorber size ($l(\text{O VI})$). Absorber size is calculated in the bottom panel of Figure 7 by dividing the column density by the number density of O VI:

$$l(\text{O VI}) = \frac{N(\text{O VI})}{n_{\text{H}}(\text{O VI}) \frac{Z_{\text{O}}}{f_{\text{H}}} \frac{m_{\text{H}}}{m_{\text{O}}} f(\text{O VI})} \text{ cm} \quad (10)$$

where the $f_{\text{H}} = 0.76$ is the mass fraction in hydrogen, and $\frac{m_{\text{H}}}{m_{\text{O}}}$ is the ratio of the atomic weights (0.0625). Absorbers remain between 50-100 kpc at $N(\text{O VI}) < 10^{14.0} \text{ cm}^{-2}$ where $f(\text{O VI}) \approx 0.20 - 0.25$, and rise to many hundreds of kpc at $N(\text{O VI}) = 10^{14.5} \text{ cm}^{-2}$ assuming photo-ionization. The large required path length for the very strongest absorbers makes photo-ionized absorbers rarer, and makes collisionally ionized systems ($T = 10^{5.45}$) with smaller sizes (red curve) more viable. We will discuss such systems further in §5.3.

In summary, virtually all O VI IGM absorbers are photo-ionized. Weak absorbers trace filaments with overdensities in the range of 10 – 20; intermediate absorbers trace overdensities 20 – 100; and strong absorbers trace gas within or near galactic halos. We stress that some collisionally ionized O VI absorbers do exist, particularly for the strongest absorbers where a much shorter pathlength can yield sufficient $N(\text{O VI})$, but these are better viewed as galactic halo rather than IGM absorbers. Strong O VI absorbers associated with the MW halo indicate collisionally ionized oxygen, because otherwise their long pathlengths would be unable to fit within the halo (Sembach et al. 2003); our absorber length analysis agrees with this assessment. Since our sight lines occasionally pass through such halos, we discuss such absorbers in §5.3 when we consider environment. Finally, while we have used the d32n256vzw150-bturb model, the trends identified here are nearly identical without sub-SPH turbulence added, and are essentially independent of wind

model. In other words, the photo-ionized nature of IGM O VI absorbers is a highly robust prediction of our simulations.

4.2 Cooling Times

The inhomogeneous nature of the metal distribution is vital for the photo-ionizational explanation of O VI, because metal-line cooling (which we implemented in GADGET-2 in OD06) is much more effective when metals are concentrated. Consider the cooling time of gas in CIE at $z = 0.25$:

$$\tau_{\text{cool}} = 4.12 \times 10^{-17} \frac{T}{\delta \Lambda(T, Z)} \text{ yrs} \quad (11)$$

where Λ is the cooling rate ($\text{ergs s}^{-1} \text{ cm}^3$)³. Let us consider the cooling time of a typical $10^{13.0} \text{ cm}^{-2}$ absorber (corresponding to overdensity, $\delta = 13$), assuming it cools from 3×10^5 K. If we use \bar{Z} from Equation 9 (i.e. we assume the mean IGM metallicity) and assume solar abundance ratios for all species, the cooling time is 42 Gyr. Conversely, using the metallicity of O VI absorbers from Equation 8 yields a cooling time of 10 Gyr. Hence weak absorbers cannot cool significantly within a Hubble time at the mean metallicity, but can do so at the mean O VI absorber metallicity. Similarly, a strong system with $N(\text{O VI}) = 10^{14.5} \text{ cm}^{-2}$ ($\delta \sim 100$) has cooling times for a mean IGM metallicity and for O VI absorber metallicity of $\tau_{\text{cool}} = 2.9$ and 0.6 Gyr, respectively. Of course, densities in the early Universe were higher by $(1+z)^3$, and cooling times depend inversely, but metallicities were lower, so these cooling times are probably overestimates. Still, for observed O VI absorbers the cooling time is generally shorter than a Hubble time (τ_{Hubble}) when the O VI absorber metallicity is considered.

Weaker absorbers take longer to cool, but as we will show in §5.1 weak absorbers trace some of the oldest metals injected at high- z , while stronger absorbers trace more recent metal injection. This means that all but the very strongest O VI absorbers have had plenty of time to cool to photo-ionized temperatures since their injection into the IGM. Physically, this is why the clumpy metal distribution where $Z \sim 5\bar{Z}$, causes most O VI absorbers to be photo-ionized.

In practice, superwind feedback shock-heats metals to higher temperature ($T > 10^6$ K) in denser environs than those traced by photo-ionized O VI. The result is a range of cooling times with lower metallicities more likely to have $\tau_{\text{cool}} > \tau_{\text{Hubble}}$ and remain in the WHIM or hot IGM, and higher metallicities often with $\tau_{\text{cool}} \ll \tau_{\text{Hubble}}$. This latter case includes metals traced by photo-ionized O VI. The strength of the feedback is a sensitive determinant for which (ρ, T) path an SPH particle will follow, with stronger feedback putting many more metals into the WHIM and hot IGM (OD08). Our main point here is to show that metals heated to WHIM temperatures at O VI absorber metallicities will usually cool to photo-ionized temperatures by today.

³ See Gnat & Sternberg (2007) for a derivation of the general form of this formula.

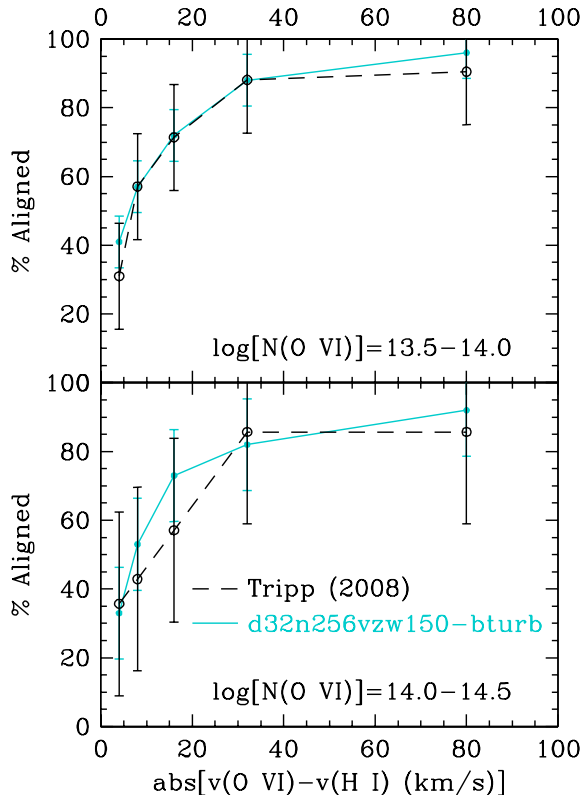


Figure 8. The alignment fraction of O VI absorbers with H I at various separations in two bins covering intermediate absorbers ($N(\text{O VI}) = 10^{13.5-14.0}$ and $10^{14.0-14.5} \text{ cm}^{-2}$). The T08 data is compared to the $S/N = 10$ sight lines of the d32n256vzw150-bturb simulation, showing nearly perfect agreement in the lower bin (top) and adequate agreement in the upper bin (bottom). The high aligned absorber fractions are an indication of photo-ionized O VI.

4.3 Alignment with H I

We have thus far discussed O VI absorbers independently of H I. Any model for O VI absorbers should also reproduce the general properties of *aligned* H I absorbers, in addition to reproducing global Ly α forest properties (e.g. Davé et al. 1999; Davé & Tripp 2001). We start by emphasizing that a vast majority of O VI absorbers are aligned at some level with H I. However, from the H I- and O VI-weighted density and temperature of well-aligned absorbers, we will demonstrate that aligned absorbers often arise in different phases of gas. We introduce the idea of multi-phase photo-ionized models with different density and temperatures for the O VI and H I components. We then estimate H I-derived absorber length, showing these can differ from the O VI lengths often because they are tracing different phases of gas. Lastly, we fit multi-phase ionization models to the $N(\text{H I}) - N(\text{O VI})$ plane, to understand what types of absorbers populate various regions. This can aid in interpretation of data sets such as T08 and upcoming data from COS.

The alignment fraction as a function of velocity separation for this model, as for most of our models, agrees well with observations, as we show in Figure 8 for intermediate absorbers split into two bins. Well-aligned absorbers ($\delta v \leq 8 \text{ km s}^{-1}$ or $\leq 100 \text{ kpc}$ in a Hubble flow) comprise 57% of all O VI absorbers in the d32n256vzw150-bturb simula-

tion when considering intermediate absorbers, in statistical agreement with T08 (54%) (see §3.2). We use the $S/N = 10$ lines of sight in this case, because it is more similar to the data S/N ; the high quality sample has a 62% alignment fraction, since more components are identified. The agreement in the $N(\text{O VI}) = 10^{13.5-14.0} \text{ cm}^{-2}$ bin is nearly perfect. There are fewer aligned absorbers in the data for the higher column density bin ($N(\text{O VI}) = 10^{14.0-14.5} \text{ cm}^{-2}$), but this is not a statistically significant difference since the observed sample has only 14 absorbers.

Misaligned absorbers are an important population, being a signature of collisionally ionized O VI as we discuss in §5.3. Our discussion in that section suggests strong absorbers have a greater chance of being collisionally ionized; however we argue in the following subsections that the high number of aligned absorbers in both the data and simulations is a strong indication of photo-ionized O VI.

4.3.1 Density and Temperature

While we have argued that the vast majority of O VI absorbers are aligned at some level (e.g. Thom & Chen 2008a), do such aligned absorbers trace the same underlying gas? To answer this we plot the H I and O VI-weighted densities and temperatures for well-aligned absorbers against each other in Figure 9. H I and O VI trace the same density gas below $n_{\text{H}} \approx 10^{-4.8} \text{ cm}^{-3}$, but above this the absorbers tend to become multi-phase in density. The declining ionization fraction of photo-ionized O VI makes it a poor tracer of gas inside halos at overdensities above a couple hundred. These rare instances are less represented in well-aligned O VI absorbers due to the large peculiar velocities of various components. However, the spatial extent of regions at overdensities ~ 500 traced by strong H I is small ($< 100 \text{ kpc}$), and gas at lower overdensities tracing strong O VI absorption is often close by and therefore appears aligned.

The weighted temperatures show significantly less alignment, and reveal something that may be counter-intuitive – metal-enriched gas is cooler than unenriched gas. It is counter-intuitive in the sense that to reach the IGM via superwind feedback, gas is driven at high velocities and therefore must shock heat. However, stronger metal-line cooling outweighs this by low- z . The H I temperatures span a wider range, just falling short of the $T = 10^5 \text{ K}$ limit, which enters the realm of BLAs ($b(\text{H I}) = 40 \text{ km s}^{-1}$). The two temperatures show that even in aligned absorbers at similar densities, O VI and H I are not tracing the same gas. Again, we suggest that O VI is arising from a clumpy distribution that picks out enriched regions of the more smoothly varying Ly α forest. Several rare instances of O VI in CIE is aligned with cooler gas with H I absorption.

4.3.2 Absorber Size

Before introducing ionization models predicting line ratios, we must consider the H I-weighted absorber size, which is different than $l(\text{O VI})$. We show the H I-weighted density for all H I absorbers, even those without O VI, in the top panel of Figure 10. A fit to the median of these absorbers between $N(\text{H I}) = 10^{12.0-14.5} \text{ cm}^{-2}$ gives the relation

$$\log[n_{\text{H}} (\text{cm}^{-3})] = -15.68 + 0.77 \log[N(\text{H I})] \quad (12)$$

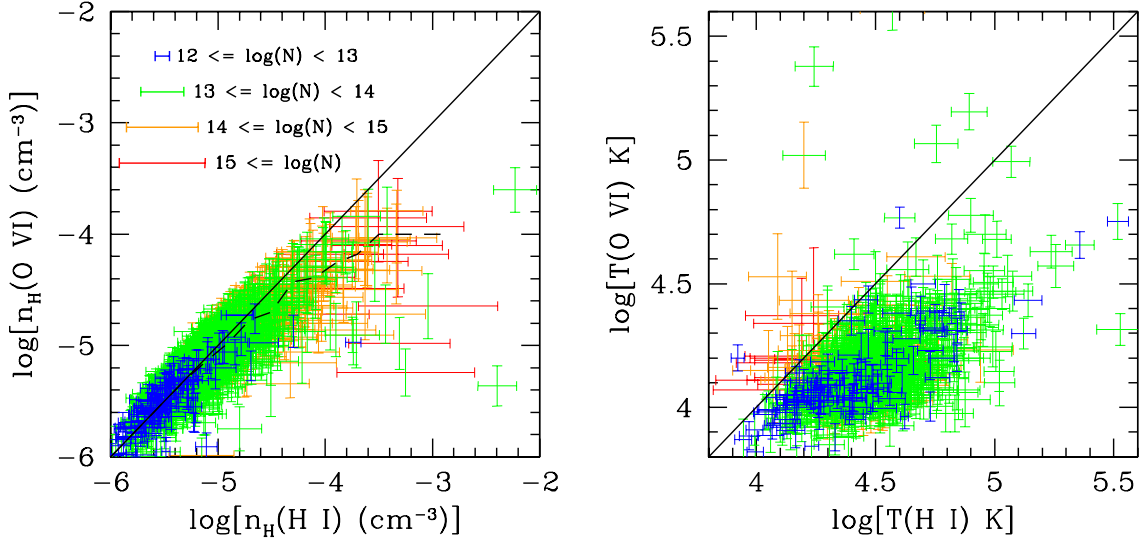


Figure 9. The multi-phase nature of well-aligned absorbers is shown by plotting H I and O VI-weighted temperatures and densities against each other (left & right panels respectively) from 70 sight lines. The column density of absorbers are indicated by both the size and color of the error bar with $N(\text{H I})$ in the x direction and $N(\text{O VI})$ in the y direction. Densities diverge above $n_{\text{H}} = 10^{-4.8} \text{ cm}^{-3}$ where O VI more often traces gas outside halos while H I traces gas within. The dashed line indicates the relation we use between the two densities. Temperatures are generally cooler for metal-enriched gas indicating metal-line cooling plays an important factor in gas, which indicates an inhomogeneous distribution of metals.

at $\langle z \rangle = 0.25$, and well describes the lower density boundary of H I absorbers over 7 orders of magnitude. This relationship is also derived by Davé et al. (1999), finding $\log(n_{\text{H}}) = -15.13 + 0.7 \log[N(\text{H I})]$ at $z = 0.25$, and analytically by Schaye (2001) by assuming the characteristic size of an absorber is well-described by the IGM Jeans length, $\log(n_{\text{H}}) = -14.68 + 2/3 \log[N(\text{H I})]$. Our current simulations (which are much improved over Davé & Tripp 2001) find an overall slightly steeper dependence and a higher normalized n_{H} . The upward scatter in the top panel of Figure 10 are the absorbers likely to be part of complex H I systems; similar scatter is seen by Davé & Tripp (2001). The well-aligned absorbers plotted in the bottom of Figure 10 are consistent with equation 12 (red line), showing that they generally are not a biased population of H I absorbers, except that stronger H I is more likely to have aligned O VI⁴.

We take Equation 12 as the relation between $N(\text{H I}) - n_{\text{H}}$ for all aligned absorbers, despite the scatter, and use the H I fraction for gas at $T = 10^{4.3} \text{ K}$ photo-ionized by a quasar-dominated ionization background, $\log[f(\text{H I})] = 0.17 + 0.99 \log(n_{\text{H}})$, to get the neutral hydrogen column density relationship:

$$\log[N(\text{H}) (\text{cm}^{-2})] = 20.19 + 0.31 \log(n_{\text{H}}). \quad (13)$$

Dividing $N(\text{H})$ by n_{H} yields the absorber length,

$$\log[l(\text{H I}) (\text{cm})] = 20.19 - 0.69 \log(n_{\text{H}}). \quad (14)$$

We plot $l(\text{H I})$, using the assumption that $n_{\text{H}}(\text{O VI}) = n_{\text{H}}(\text{H I})$ as an orange dash-dot line in Figure 7 to contrast with the O VI-derived absorber size, 50 – 100 kpc at $N(\text{O VI}) < 10^{14.5} \text{ cm}^{-2}$. Below $N(\text{O VI}) = 10^{14.0} \text{ cm}^{-2}$, it seems fair to assume the same densities since $n_{\text{H}} <$

$10^{-4.5} \text{ cm}^{-3}$, and the resulting O VI absorber lengths fit within the H I absorber lengths. Above $10^{14.0} \text{ cm}^{-2}$, $l(\text{H I})$ becomes shorter than $l(\text{O VI})$ for several reasons. First and perhaps most important, the densities where the two species arise diverge above $n_{\text{H}} = 10^{-4.8} \text{ cm}^{-3}$, with O VI arising from lower density gas distributed over larger lengths. Second, stronger absorbers are less likely to be aligned due to larger peculiar velocities, making this comparison less meaningful. Third, strong absorbers are more likely to have metals at CIE temperatures, raising the ionization fraction and lowering $l(\text{O VI})$. Finally, the successive scatter in each step above to get $l(\text{H I})$ adds up when considering the spread in temperatures.

As an interesting aside, we investigate the “ $N(\text{H})$ conspiracy” for low- z metal line systems presented by Prochaska et al. (2004). They find six O VI absorbers in the PKS 0405-123 spectrum averaging $N(\text{H}) = 10^{18.7} \text{ cm}^{-2}$ with a scatter of only 0.3 dex. In fact, this is straightforwardly understood in the context of our photo-ionized model for O VI absorbers. The $N(\text{H})$ conspiracy comes about because O VI arises mostly from photo-ionized overdensities ($\sim 10 - 200$ at $z = 0.25$), which leads to a similarly small range, $N(\text{H}) = 10^{18.50-18.91} \text{ cm}^{-2}$ (using eq. 13), in our model. This range is in excellent agreement with Prochaska et al. (2004), providing further evidence that O VI in our simulations is tracing the cosmic web as observed. $N(\text{H})$ column densities below $10^{18.5} \text{ cm}^{-2}$ generally indicate photo-ionized absorbers according to Richter et al. (2006).

A common method to estimate oxygen metallicities of aligned absorbers from observations is

$$Z_{\text{O}} = \frac{N(\text{O VI})}{N(\text{H I})} \times \frac{f(\text{H I})}{f(\text{O VI})} \times \frac{m_{\text{O}}}{m_{\text{H}}} \times f_{\text{H}}. \quad (15)$$

Unfortunately, this may significantly mis-estimate the true metallicity. To illustrate this, we plot this “observed metallicity” as the orange dash-dotted line in the central panel

⁴ See the end of §5.2 for the predicted fraction of H I absorbers with O VI.

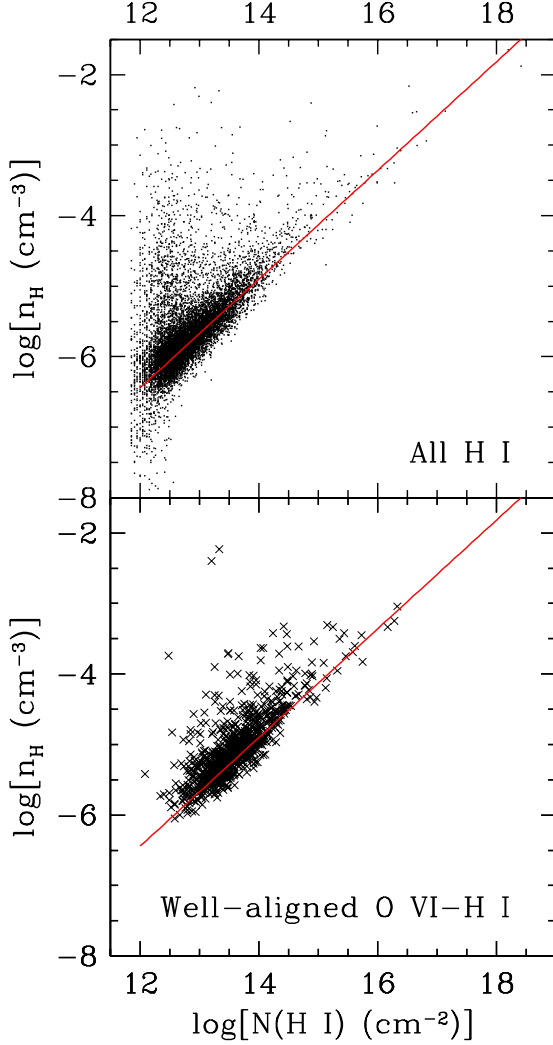


Figure 10. The H I column density is related to n_{H} over 7 decades as shown by the fit to the median density between $N(\text{H I}) = 10^{12.0-14.5} \text{ cm}^{-2}$. H I absorbers aligned with O VI follow this relation as well, however in both cases scatter exists as weak absorbers sometimes trace high densities in complex systems. The $n_{\text{H}} - N(\text{H I})$ relation is used to determine the H I-derived absorber size.

of Figure 7. At weak O VI column densities, the metallicity is underestimated, while at above $N(\text{H I}) > 10^{14.0} \text{ cm}^{-2}$ it overestimates the actual metallicity.

In summary, the H I properties of well-aligned O VI absorbers are fairly similar to general H I absorber properties. H I and O VI absorber sizes can be substantially different in stronger absorbers, because even aligned H I and O VI arise in different phases of gas. Finally, $N(\text{H})$ remaining relatively invariant over a large range of $N(\text{O VI})$ is expected if well-aligned absorbers arise from typical H I absorbers.

4.3.3 Ionization Models

Having the length scale of aligned absorbers, along with densities and temperatures, we now have everything necessary to fit ionization models to O VI – H I line ratios. This is portrayed in Figure 11 using the $N(\text{H I}) - N(\text{O VI})$ multi-phase

plane considered by Danforth & Shull (2005) and T08. Note that these authors plot $N(\text{H I})$ versus $N(\text{H I})/N(\text{O VI})$; we prefer to plot the column densities against each other directly and not the ratio, because it is simpler and makes trends clearer. Small points represent simulated aligned absorbers. We plot colored lines for various two-temperature, multi-phase models where oxygen is either photo-ionized ($T(\text{O VI}) = 10^{4.2} \text{ K}$) or in CIE ($T(\text{O VI}) = 10^{5.45} \text{ K}$), and H I is one of several different temperatures. Our models use the $z = 0.25$ metallicity-density relation (Equation 9) shown on top (dashed lines), but we also consider metallicities $5 \times \bar{Z}$ (solid lines) as more relevant given the O VI absorber metallicities from §4.1. It is difficult to create photo-ionized O VI absorbers with column densities much greater than $10^{14.3} \text{ cm}^{-2}$ using the $5 \times \bar{Z}$ relation, because $f(\text{O VI})$ declines as $N(\text{H I})$ rises creating a maximum in $N(\text{O VI})$.

The CIE models (orange, red, & magenta) follow the behavior highlighted by Danforth & Shull (2005) where $N(\text{O VI})$ is independent of $N(\text{H I})$, which sweeps across a broad swath of this plot. In our case, the H I temperature ranging from $T = 10^{4.2} \rightarrow 10^{5.5} \text{ K}$ is the variation that allows this scenario to explain most of the T08 well-aligned absorbers ($\delta v \leq 8 \text{ km s}^{-1}$ separation, blue squares) while O VI is always collisionally ionized. This scenario seems somewhat implausible at face value. Meanwhile, the photo-ionized models with two choices of $T(\text{H I})$ (cyan and green) bracket the majority of H I-derived temperatures in Figure 9, and also can explain most, *but not all*, of the T08 absorbers. Lastly, we introduce a multi-density model assuming $T = 10^{4.2} \text{ K}$ (purple) for densities above $n_{\text{H}} = 10^{-4.5} \text{ cm}^{-3}$ where we assume different absorber lengths for O VI and H I by plugging in the divergent density relationship from Figure 9 (dashed line) into Equation 14. This results in longer absorber pathlengths for O VI than H I. Unless otherwise noted, we assume aligned absorbers are described by photo-ionization.

We compare the number densities of O VI systems to aligned T08 absorbers in three bins denoted by the vertical gray lines in Figure 9– $N(\text{H I}) < 10^{13.4}$, $10^{13.4-15.0}$, and $> 10^{15.0-17.0} \text{ cm}^{-2}$, and we overlay our high quality sample of 70 lines of sight (black dots, $T(\text{O VI}) < 10^5 \text{ K}$; red dots, $T(\text{O VI}) \geq 10^5 \text{ K}$). Our sample covers $\Delta z = 35$ with $\sim 90\%$ completeness at $N(\text{O VI}) = 10^{13.0} \text{ cm}^{-2}$. We directly compare with the T08 dataset only for absorbers of at least intermediate strength, for which they have $\Delta z = 2.62$ (their effective pathlength at $EW = 30 \text{ mÅ}$).

Beginning with the strongest H I bin first, T08 finds 5 such absorbers ($1.9 \Delta z^{-1}$), which is nearly 2σ more than we find ($14, 0.4 \Delta z^{-1}$). These absorbers correspond to gas in and around halos, and rarely fall below $N(\text{O VI}) = 10^{13.6} \text{ cm}^{-2}$ in either set. Two of T08’s absorbers and many of our absorbers are above the solid $T(\text{H I}) = 10^{4.2} \text{ K}$ photo-ionized model (cyan) which seemingly rules out photo-ionization, because higher metallicities are required. We suggest that a subset of these absorbers are best described by the multi-density photo-ionized model (purple), with O VI arising from longer absorbers outside a halo, while H I traces denser halo gas. The higher observed frequency of strong absorbers in the data may indicate non-uniformity in the ionization background, where halo substructure unresolved in our simulations increases the number of absorbers

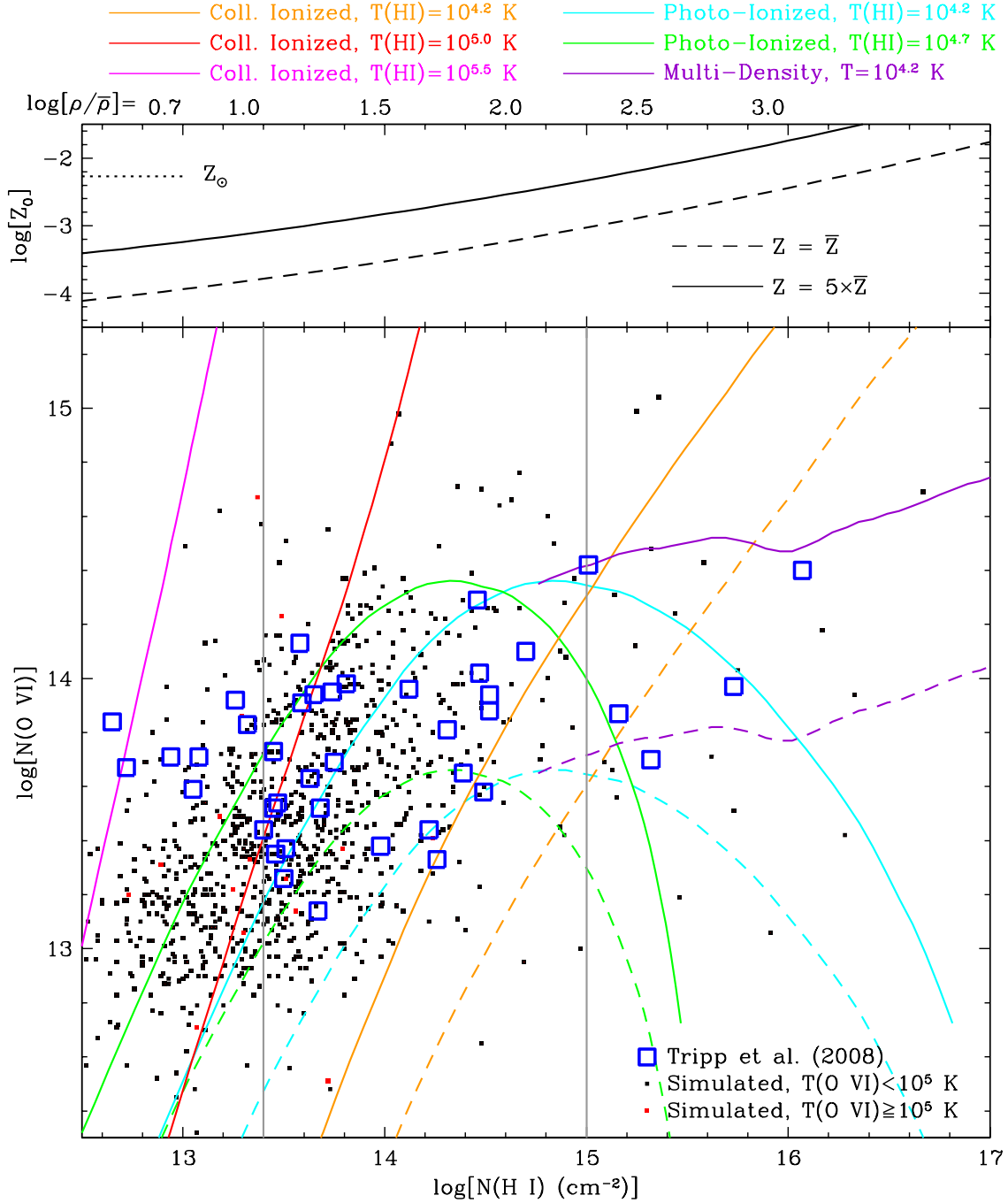


Figure 11. The $N(\text{H I}) - N(\text{O VI})$ plane shows the aligned absorbers from our high-quality lines of sight (black points, $T(\text{O VI}) < 10^5$ K; red points, $T(\text{O VI}) \geq 10^5$ K) along with absorbers observed by T08 (open blue squares). Several ionization models (colored lines) are shown using either the metallicity-density relationship, \bar{Z} , in our $z = 0.25$ d32n256vzw150 simulation (dashed lines) or $5 \times \bar{Z}$ (solid lines) since metals in O VI absorbers appear to be significantly above the cosmic average. The top panel shows this relationship translated to $N(\text{H I})$ using Equation 12 and the relation $n_{\text{H}} = 3.63 \times 10^{-7} \rho/\bar{\rho} \text{ cm}^{-3}$, which applies at $z = 0.25$. Collisionally ionized O VI ($T(\text{O VI}) = 10^{5.45}$ K) aligned with H I at various temperatures (orange, red, & magenta) can explain most absorbers, but the absorbers are vastly photo-ionized and better explained by cyan and green ionization models ($T(\text{O VI}) = 10^{4.2}$ K). The purple ionization models are multi-density with O VI arising from lower densities than H I when $n_{\text{H}} \geq 10^{-4.8} \text{ cm}^{-3}$.

with $N(\text{H I}) > 10^{15} \text{ cm}^{-2}$, which our simulations under-predict.

It is significant that few of our simulated absorbers and none of T08's correspond to values lie below \bar{Z} in either of the single-phase models (green and cyan dashed lines) above

$N(\text{H I}) = 10^{15} \text{ cm}^{-2}$, although these should be detectable in the data; this behavior also exists in the Thom & Chen (2008a) dataset. The H I often traces halo gas while the photo-ionized O VI arises from a longer pathlength of gas at $\delta \sim 100$, increasing the chance of intersecting with a

clump of metals well above \bar{Z} . Only 29% of our strong H I absorbers have well-aligned O VI, but 87% of them have O VI within 80 km s⁻¹ (see the end of §5.2 for more statistics). Our interpretation is there is almost always O VI with strong H I, but the O VI is much more extended and peculiar velocities dominate, resulting in well-aligned strong H I absorbers often being chance alignments.

We find a vast majority of aligned absorbers in the intermediate bin ($8.5 \Delta z^{-1}$), within the Poisson errors of T08 ($7.3 \Delta z^{-1}$). Most of our absorbers including those down to our detection limit fall between $1 - 10\bar{Z}$, which should happen according to our photo-ionized O VI model. These absorbers tracing $\delta = 10 - 100$ are more likely to be associated with hotter H I, for which the $T(\text{H I}) = 10^{4.7}$ K photo-ionized model may be more relevant. This model encompasses a cluster of T08 absorbers with $N(\text{H I}) \approx 10^{13.4-13.6}$ cm⁻², which is near the the peak concentration of our simulated absorbers. Sub- \bar{Z} absorbers should theoretically exist in this bin, although it is rare for metallicities traced by O VI to fall below \bar{Z} . Part of this discrepancy may be explained by smaller $l(\text{O VI})$ (~ 50 kpc) aligned with greater $l(\text{H I})$ (~ 100 kpc), underestimating the true metallicity. COS should help confirm or exclude the presence of low-metallicity O VI absorbers.

The lowest strength aligned absorbers are slightly under-predicted by our simulation ($1.9 \Delta z^{-1}$) relative to the T08 dataset ($3.1 \Delta z^{-1}$, a 1.1σ difference). Four of 7 T08 weak aligned absorbers are in simple systems, and bear a resemblance to their proximate absorbers with $N(\text{H I}) < 10^{13.0}$ cm⁻². The O VI column densities are at least $\times 3$ greater than the H I in the data in every case, which is true only a quarter of the time for the simulated absorbers. We suggest the possibility of a non-uniform ionization background at the Lyman limit due to the proximity of AGN could result in weaker H I for an absorber, while $N(\text{O VI})$ remains unchanged, because the 8.4 Rydberg ionization field is more uniform as these photons have a much longer mean free path. This could push a number of aligned absorbers from the middle H I bin into the lowest bin in Figure 11.

We find 5.1 absorbers per Δz where $N(\text{H I}) < 10^{13.4}$ cm⁻² and $EW(\text{O VI}) = 10 - 30$ mÅ, whereas there are none observed by T08. COS should be able to access such absorbers, which should indicate the enrichment level of the IGM at overdensities of 5-10.

Considering strong O VI absorbers ($N(\text{O VI}) \geq 10^{14.5}$ cm⁻²) with aligned H I, we find 14 ($0.4 \Delta z^{-1}$) while T08 finds none. These absorbers are predominantly photo-ionized, but excluded by our ionization models, because the metallicity would have to be at least $10\bar{Z}$ in most cases, which rarely occurs. Most of these absorbers fall off the $N(\text{H I}) - n_{\text{H}}$ relation from Equation 12 indicating they they are part of a complex system with significant peculiar velocities, and possibly chance alignments. Finding no such absorbers in the data, we may be overestimating the O VI columns of such strong absorbers as we discuss in §5.3.

To summarize, an in-depth examination on the $N(\text{H I}) - N(\text{O VI})$ plane shows we can explain some trends in the data with our photo-ionized multi-phase explanation, most importantly that O VI appears to rise quite gradually with increasing H I (cf. Figure 1 of Danforth & Shull 2005). Our absorbers however appear more clustered at $N(\text{H I}) = 10^{13.5-14.5}$ cm⁻² compared with the T08 dataset, and we

believe a varying ionization background near 1 Rydberg is the best way to distribute over a wider range of H I column density. We encourage the use of *Hubble*/COS to greatly expand the aligned H I – O VI weak absorber statistics, as these are one of the most straight-forward and effective ways to constrain ionization conditions of metals and the enrichment levels of filamentary structures ($\delta \sim 10$).

4.4 Turbulence in the IGM

By forwarding the d32n256vzw150-bturb model, we are claiming that there is some form of turbulence in the low- z IGM well below the resolution of our simulation that is responsible for broad O VI lines. We arrive at this claim by exploring every other broadening mechanism (spatial, temperature, and instrumental), and finally settling on sub-SPH motions as the only viable explanation. We use “turbulence” as a blanket term to cover velocity shear, bulk motions, shock disturbances, and other random motions unresolvable in our simulations. Our main point is that such motions increasingly dominate the line profiles for stronger low- z O VI absorbers. In this section we connect (circumstantially, at least) turbulence to the outflows that enrich and stir the IGM. We begin by showing that examples of turbulence in the IGM and halo gas are common, and then use simple physical relations from Kolmogorov (1941) turbulence to broadly motivate our prescription of sub-SPH turbulence.

Turbulence or some other non-thermal broadening is commonly invoked to explain O VI line widths in the IGM (e.g. Danforth et al. 2006). Aligned H I – O VI absorbers allow a constraint on how much of a b -parameter is thermal and non-thermal. Both T08 and Thom & Chen (2008b) agree that such systems almost always have $T < 10^5$ K, with non-thermal broadening significant if not dominant. Even in our models without turbulence, the same exercise reveals a significant non-thermal broadening, a finding also confirmed in the simulations of Richter et al. (2006). However, such alignments do not *necessarily* imply turbulent motions, and instead may only indicate that metal absorbers arise from different gas than H I.

A more relevant measurement may be aligned H I – He II components, which do not rely on the metal distribution, and have been shown by Zheng et al. (2004) to indicate the IGM is dominated by turbulence at $z = 2 - 3$. Fechner & Reimers (2007) downplay the amount of turbulence in the IGM, finding that only 45% of such aligned components favor turbulent broadening. Our invocation of turbulence requires the association with outflows and metals; therefore we disfavor turbulence in the low-density, diffuse IGM, which is likely unenriched. Furthermore, Davé & Tripp (2001) show that the low- z Ly α forest is well described by thermal line widths alone, and we reaffirm this point by showing in §3.1 that lines with $N(\text{H I}) < 10^{14}$ cm⁻² are unaffected by our addition of turbulence.

A more direct way to measure turbulence is to look for velocity differences on the smallest scales possible, as Rauch et al. (2001) did in lensed quasars. By observing adjacent C IV profiles in paired lines of sights, they find $\delta v \sim 5$ km s⁻¹ on scales of 300 pc at $\langle z \rangle \sim 2.7$. They apply the Kolmogorov steady-state assumption whereby kinetic energy, $\frac{1}{2}\langle v_{KE}^2 \rangle$, injected at a rate ϵ_0 cascades through

increasingly small eddies at $\epsilon \approx \epsilon_0$ until viscosity transforms this energy to heat. The dimensionless nature of Kolmogorov turbulence allows the application of a simple scaling between size, l , and rms velocity, v_{rms} , such that $\bar{v}_{\text{rms}}^2 \approx (\epsilon l)^{2/3}$. Therefore, similar to Rauch et al. (2001), we use the energy transfer rate $\epsilon \approx v_{\text{rms}}^3/l$ to parametrize turbulence. For O VI absorbers we assume $\bar{v}_{\text{rms}} \sim b_{\text{turb}}$ and the transverse $l \sim l(\text{O VI})$, such that

$$\epsilon \sim \frac{b_{\text{turb}}^3}{l(\text{O VI})}. \quad (16)$$

This application of transverse δv 's to b -parameters makes more sense for O VI, because O VI has been shown to be distributed on scales much larger than a kpc whereas lower ionization species (e.g. C IV, C III, Si IV) show sub-kpc structure indicating small cloudlets (Lopez et al. 2007). Therefore, a single broad O VI profile may comprise many small metal-enriched cloudlets traced by low ionization species of the sort suggested by Simcoe et al. (2006) and Schaye et al. (2007). In this scenario O VI traces more extended metals at lower densities where turbulence on scales of 50-100 kpc dominates the line width, while small, dense cloudlets traced by low ionization species, possibly in sub-kpc clouds, show less broadening due to the Kolmogorov scaling. The result is the type of low- z system commonly observed, where low ionization species have multiple thinner profiles along with one large broad O VI profile (e.g. Thom & Chen 2008b), which we suggest may be primarily photo-ionized. This is only a hypothesis, and should be tested in galactic-resolution simulations where turbulence and the formation of dense clumps can be better resolved.

Rauch et al. (2001) calculates $\epsilon \sim 10^{-3} \text{ cm}^2 \text{ s}^{-3}$ for high- z C IV absorbers, and uses the dissipation timescale,

$$\tau_{\text{diss}} \sim \frac{\langle v_{\text{KE}}^2 \rangle}{2\epsilon} \quad (17)$$

to find that the turbulence should dissipate in $\approx 10^8$ yrs. The average velocity of the kinetic energy input, $\langle v_{\text{KE}} \rangle$, is speculated to arise from some sort of galactic-scale feedback. This short timescale, along with C IV arising from overdensities enriched recently by SF galaxies (OD06), indicates a more violent environment than the overdensities O VI absorbers trace at low- z ; therefore we consider this energy transfer rate an upper limit for low- z O VI. We calculate and plot ϵ as a function of $N(\text{O VI})$ in the central panel of Figure 12 for both the photo-ionized and CIE cases by assuming b_{turb} from the top panel and $l(\text{O VI})$ from the bottom panel of Figure 7.

If we use photo-ionized absorber lengths below $10^{14.5} \text{ cm}^{-2}$ ($l(\text{O VI}) \sim 50 - 100 \text{ kpc}$), we find energy transfer rates at most $\sim 2 \times 10^{-4} \text{ cm}^2 \text{ s}^{-3}$ dropping rapidly at lower $N(\text{O VI})$. $l(\text{O VI})$ grows rapidly above $10^{14.5} \text{ cm}^{-2}$ for photo-ionized absorbers reducing ϵ , but the absorber length from O VI in CIE compresses such absorbers to be $\ll 100 \text{ kpc}$, so that these absorbers (often tracing halo gas) are able to fit within a halo. ϵ grows to match the Rauch et al. (2001) value for the strongest O VI absorbers. Such absorbers we will argue in §5.3, may be analogous to the O VI absorbers associated with the MW halo and thick disk, which must be collisionally ionized (Sembach et al. 2003; Fox et al. 2004). Considering the thick disk absorbers with 60 km s^{-1} corresponding to a structure on at most several

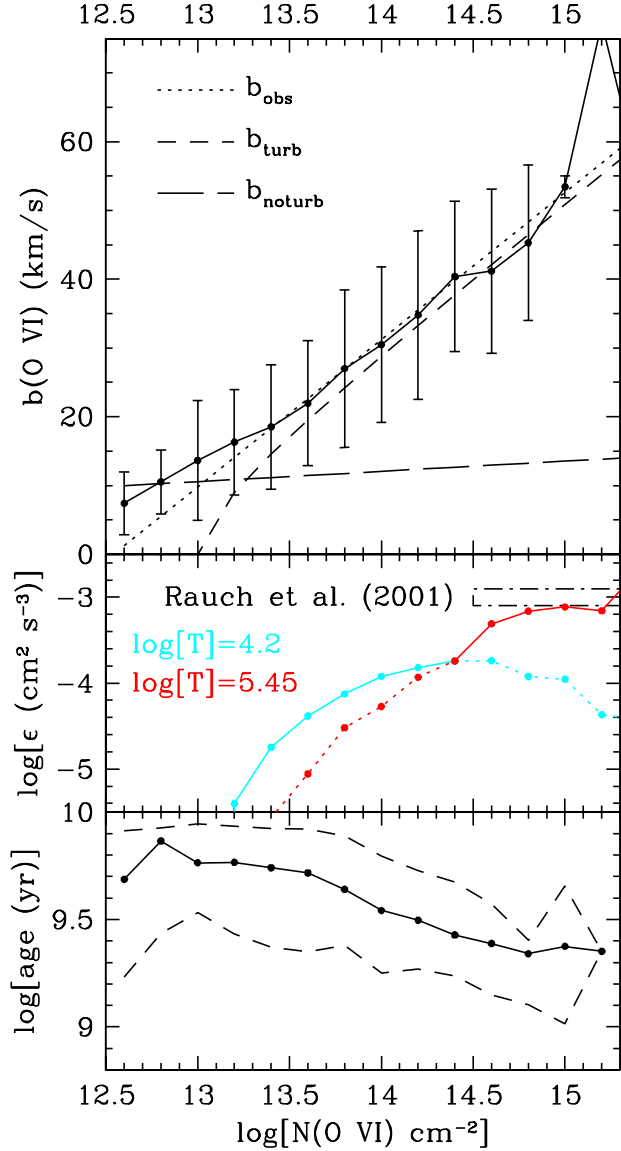


Figure 12. The b -parameters from the d32n256vzw150-bturb model are plotted as data points with 1σ dispersions. b_{obs} is a linear fit to the T08 $b(\text{O VI}) - N(\text{O VI})$ relation, and b_{noturb} is the fit to the d32n256vzw150 model. From these fits, the relation for b_{turb} is calculated in Equation 5. If we consider the photo-ionized and collisionally ionized absorber sizes in the bottom panel of Figure 7, we can calculate the energy dissipation rate ϵ (center panel), which indicates lower rates than observed at high- z by Rauch et al. (2001) for photo-ionized absorbers tracing the diffuse IGM. The median ages are plotted (bottom panel) to show that more turbulence may be associated with metals ejected more recently.

kpc (Savage et al. 2003), we subtract off the temperature broadening (17.7 km s^{-1} at $T = 10^{5.45} \text{ K}$), the instrumental broadening ($\sim 20 \text{ km s}^{-1}$ for FUSE), and safely assume no spatial broadening to arrive at $b_{\text{turb}} \sim 54 \text{ km s}^{-1}$. If we assume pure Kolmogorov turbulence and $l(\text{O VI}) = 3 \text{ kpc}$, we find a much higher transfer rate, $1.7 \times 10^{-2} \text{ cm}^2 \text{ s}^{-3}$. Similar size assumptions for the Sembach et al. (2003) absorbers, which are more difficult to estimate due to their less constrained distance, give $b_{\text{turb}} \sim 30 \text{ km s}^{-1}$ and $\epsilon =$

$3 \times 10^{-3} \text{ cm}^2 \text{ s}^{-3}$. These values are higher than in the IGM at $z > 2$ and within MW molecular clouds, $\epsilon \sim 4 \times 10^{-4} \text{ cm}^2 \text{ s}^{-3}$ (Larson 1981), although more similar to H II regions $\epsilon \sim 2.5 \times 10^{-2} \text{ cm}^2 \text{ s}^{-3}$ for a 100 pc-sized region (O’Dell 1991). The latter do not show a Kolmogorov spectrum, but may be more related to outflows driven by supernovae, which may include IVCs and HVCs in the MW halo. The key point here is that the turbulence we invoke for most O VI systems is a small fraction of the energy transfer rate seen at high- z and smaller still compared to turbulence associated with active regions within our Galaxy.

Do our absorbers follow a Kolmogorov spectrum? We should see evidence of an increasing b_{noturb} in the higher resolution d16n256vzw150 simulation compared to d32n256vzw150 if it is. Our added turbulence, b_{turb} from Equation 3, should be reduced by a factor of $\frac{1}{2}^{1/3} \sim 0.8$ when halving the resolved length scales according to Equation 16 if ϵ is constant; however we see no evidence of an increasing b_{noturb} with resolution. Therefore, either turbulence begins at smaller scales with a larger ϵ , or it does not follow a Kolmogorov spectrum. There may be a precedent for the former as simulations of SNe-driven ISM turbulence by Joung et al. (2008) find that energy injection occurs over a broad range of scales. The turbulent energy injection of outflows may very well occur on scales less than the resolution of our simulations ($\sim 20 - 50$ kpc for halo gas) meaning that ϵ is larger.

Why would turbulence decline toward lower overdensity? As a possible answer, we consider the ages of individual SPH particles defined by the last time they were launched in a wind. We define the average “age” of an absorber as an O VI-weighted age of its contributing SPH particles (equation 7). Plotting the median age of O VI absorbers with 1σ dispersions (bottom panel of Figure 12) shows that younger absorbers have higher column densities, which in turn have more turbulent broadening in our model. The average age of metals in a $10^{13.0} \text{ cm}^{-2}$ is about 6 Gyr while for a $10^{14.5} \text{ cm}^{-2}$, the age is 2.5 Gyr. Note that this is an *average* age, and higher column density absorbers may be composed of a number of SPH particles with a range of ages, a significant fraction of which are below 1 Gyr. Our turbulence model is therefore consistent with the idea that turbulence is injected by outflows, and then dissipated on a timescale comparable to (or perhaps somewhat shorter than) a Hubble time.

Finally, we stress the need for high-resolution simulations to trace outflows as they move from the galactic ISM into the IGM. The largest contributor of ISM turbulence in star-forming galaxies appears to be supernovae (Mac Low & Klessen 2004), with $> 90\%$ of the kinetic energy from SNe-driven turbulence contained shortward of 200 pc (Joung & Mac Low 2006). Although cosmological simulations are far from capable of resolving such scales, an implementation of a sub-grid model of turbulent pressure appears conceivable (Joung et al. 2008). Meanwhile, the simulations of Fujita et al. (2008) track the formation of shell fragments by Rayleigh-Taylor instability thought to be responsible for Na I absorption tracing wind feedback around star-forming galaxies (e.g. Martin 2005a). The differential velocities produce Na I line widths of $320 \pm 120 \text{ km s}^{-1}$, which we would describe ascribe as turbulent broadening using our broad definition. We hypothesize that the hot medium driv-

ing the shell fragments that escape into the IGM evolve into the low density metals traced by O VI with denser cloudlets traced by low ionization species (e.g. C II, C III, & Si II). Extending galactic-scale simulations, including treatment for small-scale turbulence (< 200 pc), to follow winds into the IGM under an ionizing background should help show how turbulence affects the line profiles of various species.

To summarize, “painting on” turbulence post-simulation should rightfully be considered controversial. However, it also likely to be unrealistic that gas on 20-100 kpc scales pumped by galactic outflows has no internal motions on smaller scales. The energy dissipation rate of the required turbulence at low- z is just a fraction of that observed for high- z C IV, which traces more recent SF activity. Our discussion here emphasizes that IGM metal-line absorption profiles can be dominated by small-scale velocities, analogous to the line profiles of Galactic H II regions, molecular clouds, IVCs, and HVCs. In fact, the diffuse Ly α forest may be a rare instance of something relatively unaffected by turbulent velocities. Resolution appears to resolve better some of the small scale velocities in the very strongest absorbers, but if the d16n256vzw150 simulation is any guide, the resolution required to accurately model such small-scale motions is likely much higher. Lastly, we have added turbulence as a function of density, which is only a first-order approximation for the more relevant properties of environment and ages of metals; an interesting future study (particularly in comparison to COS data) would be to see how exactly turbulence originates and what parameters best describe it.

5 ORIGIN AND ENVIRONMENT OF O VI

The primarily photo-ionized nature for O VI absorbers suggests this ion traces metals in the warm diffuse IGM. We consider here the origin of various absorbers by determining when their metals were last injected by winds. The age-density anti-correlation alluded to in the previous section naturally segues into a discussion of environment, where we consider an absorber’s relation to galaxies responsible for enriching the IGM. We then discuss collisionally ionized O VI, noting that it appears primarily within halos of $\sim M^*$ galaxies which we suggest is analogous to O VI associated with the MW galactic halo. Finally, we show simulated COS observations of O VI absorption systems, demonstrating how such observations can provide insights about environment and the evolutionary state of IGM gas.

Figure 13 illustrates various physical and observational properties of the IGM around four selected galaxies ranging over two orders of magnitude in stellar mass. These figures show zoomed-in views of some of the trends seen in Figure 1. Metals follow galaxies, and O VI in particular traces filamentary structures. Despite a large range in stellar mass in the left three columns, the extent of O VI is not qualitatively different. Furthermore, the stronger O VI in the group environment on the right panels are found around galaxies on the outskirts of this group and not around the $M_* = 10^{11.7} M_\odot$ in the center. Much of this has to do with the majority of O VI in our simulations tracing the diffuse, photo-ionized IGM rather than hot halo gas. In this section we will con-

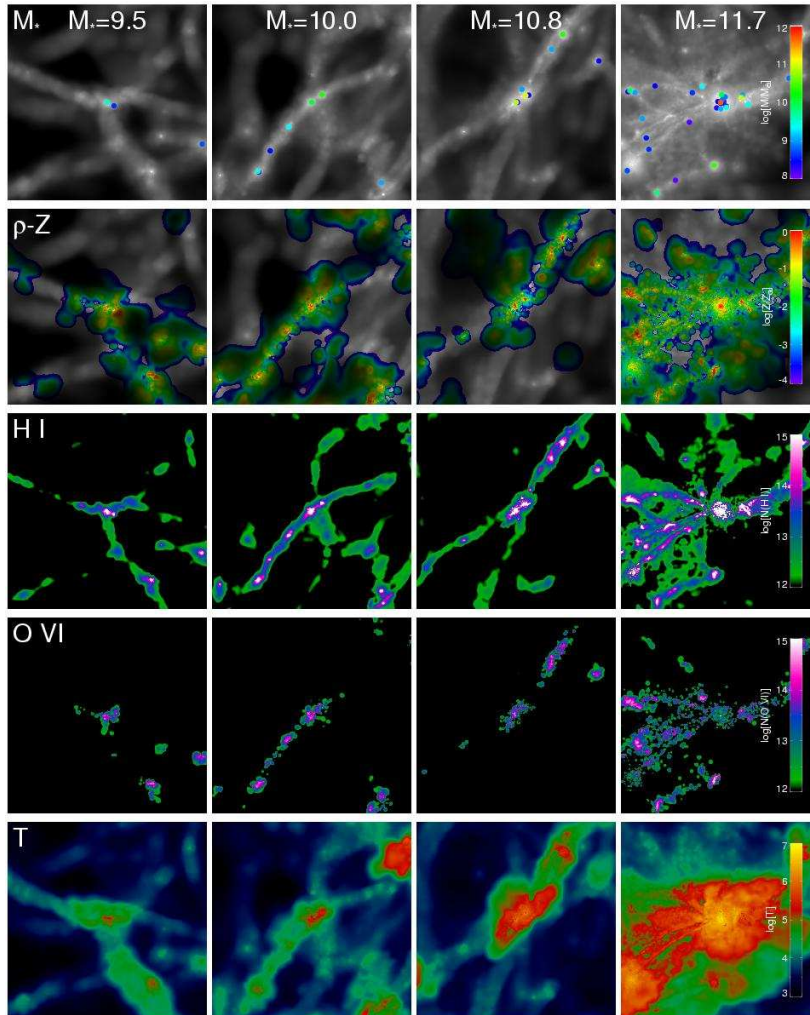


Figure 13. The IGM environments in $8 \times 8h^{-1}\text{Mpc} \times 25 \text{ km s}^{-1}$ slices around 4 different-sized galaxies at $z = 0.25$. *Top row:* Galaxy locations within the slice are indicated by colored dots corresponding to the galaxy stellar mass; the greyscale indicates gas overdensity. *Second row:* Colors indicate the enrichment level of the gas with the greyscale. *Third row:* H I column densities. *Fourth row:* O VI column densities. *Bottom row:* Average gas temperature of the IGM. Four different galaxy environments are displayed ranging from sub- L^* (left 2 columns), an L^* galaxy analogous to the Local Group (third column), and a massive group environment (last column). The strength and extent of O VI does not necessarily correlate with the galaxy mass, unlike H I. O VI is mostly photo-ionized in these simulations tracing overdensities of 10-200. Often photo-ionized O VI is co-spatial with the WHIM and hot halo gas (regions of red and yellow).

centrate on the locations of galaxies (top row) compared to O VI absorbers (4th row).

To quantify trends in origin and environment, we have modified our `specexbin` spectral generation code to assign the stellar mass (M_*) and distance (r_{gal}) to the galaxy identified via Spline Kernel Interpolative Denmax⁵ with the greatest dynamical influence for each SPH particle. Note that the d32n256vzw150 simulation resolves galaxies down to $\approx 10^9 M_\odot$. We define a *neighboring galaxy* to each SPH particle as the one with the smallest fractional virial distance to the particle (i.e. the minimum r_{gal}/r_{vir} , where $r_{vir} \propto M_{dyn}^{1/3}$). To calculate the dynamical mass (M_{dyn}) from the stellar mass we use the relation from Davé (2009), which shows the fraction of baryons in stellar mass for a given halo mass as calculated from this simulation and the

d64n256vzw150 simulation⁶. `specexbin` tracks age as well as the originating galaxy mass and launch v_{wind} for enriched outflow particles, but we limit ourselves to considering an absorber's age only, saving an in-depth analysis of the originating galaxies of absorbers for future work. The neighboring M_* and r_{gal} we refer to here often have no relation to that of the particle's originating galaxy, especially considering the processes in galaxy evolution and structural formation have altered the environments of O VI absorbers, which often trace metals released into the IGM at a much earlier time; this contrasts to the closely related galaxy-absorber connection found in simulations with the same wind model in Oppenheimer et al. (2009) at $z = 6$ where winds appear to be clearly outflowing from their parent galaxies. Unlike

⁵ SKID; <http://www-hpcc.astro.washington.edu/tools/skid.html>

⁶ See the relation in the left middle panel of this paper's Figure 1.

the normal version of `specexbin`, we only use one snapshot at $z = 0.25$ over the range of $z = 0.5 \rightarrow 0$, although the varying ionization fields and Hubble expansions are applied from the redshift along the line of sight; this explains why ages never go above 10 Gyr.

We plot O VI-weighted densities, temperatures, ages, and neighboring galaxy masses at absorber line centers in Figure 14 at $z < 0.5$ in 30 high-quality lines of sight from our d32n256vzw150-bturb model. The $\rho - T$ phase space panel (top left) reiterates our finding that most O VI absorbers are photo-ionized near $T = 10^4$ K with an easily noticeable density- $N(\text{O VI})$ correlation. The over-plotted logarithmic metallicity-weighted contours show low- z metals have either cooled to $T \sim 10^4$ K, where O VI is an ideal tracer of these diffuse IGM metals, or are much hotter, $T \gtrsim 10^6$ K, where cooling times are long. In between is the metal “zone of avoidance” where the rare O VI CIE absorber traces rapidly cooling halo gas. We provide an in-depth analysis of this region in §5.3.

5.1 Ages of O VI Absorbers

The ages of O VI absorbers in the bottom left panel of Figure 14 generally anti-correlate with density. Absorbers below $N(\text{O VI}) = 10^{14} \text{ cm}^{-2}$ (more often in simple systems) usually correspond to metals in filaments often injected during the high- z epoch of intense cosmic star formation. Strong absorbers trace metals on the outskirts of halos injected at $z < 1$, while some of the strongest absorbers near $N(\text{O VI}) = 10^{15} \text{ cm}^{-2}$ trace metals cycling in halo fountains within the virial radius as described by OD08 on timescales $\lesssim 2$ Gyr. Histograms of $\sum N(\text{O VI})$ are drawn for each property with the colored histograms stacked upon each other corresponding to the column density range; intermediate absorbers (green & orange) hold the majority of O VI in the IGM. A median age of 3 Gyrs is found with a spread of 0.6 dex. Interestingly C IV at $z = 2$ shows a similar age spread and median (~ 1 Gyr) in terms of a fraction of a Hubble time (Oppenheimer et al. 2007), which is not surprising considering that C IV at this redshift traces similar overdensities as low- z O VI (e.g. Simcoe et al. 2004; OD06).

The trend of increasing age with decreasing overdensity of metals results from the outside-in pattern of IGM enrichment. OD08 shows that winds launched at $z = 6 \rightarrow 0.5$ all travel similar distances (60-100 proper kpc), thereby allowing a galaxy to enrich a larger comoving volume at early times. The increasing mass-metallicity relationship of galaxies as the Universe evolves (cf. Erb et al. 2006; Tremonti et al. 2004) naturally results in a metallicity-density IGM gradient as later galaxies enrich gas at higher overdensities filling less comoving volume with more metal-rich gas. Therefore the outer regions traced by the weakest O VI absorbers are tracing the earliest epochs of IGM enrichment while remaining relatively unaffected by later enrichment. O VI is by far the best UV transition able to trace such regions due to its high oscillator strength, oxygen being the most copious metal, and its highly ionized state ideal for tracing low densities where there are many ionizing photons per ion⁷. Conversely, the overdense inner regions trace gas

recycled multiply in winds often not escaping from galactic halos, as described in OD08. These regions are relatively rare in a volume-averaged measurement as an absorption line spectrum, but may harbor the strongest lines with O VI in CIE.

5.2 Galaxy Environments of O VI Absorbers

The strong correlation between density and $N(\text{O VI})$ suggests a possible correlation between M_* and $N(\text{O VI})$, considering that we find more overdense environments associated with more massive galaxies at low- z in our simulations (OD08). The right panels of Figure 14 do show such a trend, but only very weakly; there is a large range of absorber strengths for a given M_{gal} . This is most easily noticed as the large area covered by O VI absorbers in the M_* -age space.

Another key variable we need to consider is distance from a neighboring galaxy, which we plot as a multiple of the virial radius, $r_{\text{gal}}/r_{\text{vir}}$, in Figure 15. Most O VI absorbers in the observed range reside several virial radii from the neighboring galaxy, suggesting they are dynamically unassociated with this galaxy. Histograms along the side for each column density bin indicate weaker absorbers lie at a greater virial distance from the nearest galaxy, which is on average less massive. The stellar mass associated with O VI absorbers is $M_{\text{gal}} \sim 10^{9.5-10} M_{\odot} \sim 0.03 - 0.1 M^*$. These same absorbers are among the oldest, suggesting merely incidental association with their present day neighboring galaxy. The absorbers at $N(\text{O VI}) < 10^{14} \text{ cm}^{-2}$ associated with $M_{\text{gal}} > 10^{11} M_{\odot}$ are similarly incidental. This is best illustrated by the chaotic structure of O VI absorbers in the right panels of Figure 13. Ganguly et al. (2008) finds a similar association of their weaker absorbers ($EW < 50 \text{ mÅ}$) with $\sim 0.1 L^*$ galaxies in the Cen & Fang (2006) simulation.

Our simulation results here are worth comparing to observations, however we note that we consider only galaxy stellar masses, not luminosities, and our detection limits are complete down to $M_{\text{gal}} = 10^9 M_{\odot}$, or $\sim 0.01 M^*$, which is better than any survey currently obtains, except very locally. Surveys by Prochaska et al. (2006) and Cooksey et al. (2008) of the galaxy-absorber connection find a large variety of environments for O VI absorbers, which could possibly support our claim that absorbers in the observed range are usually not directly associated with their neighboring galaxy. The majority of our absorbers are between 100-300 kpc from their nearest galactic neighbor, which compares favorably with observations finding the nearest projected neighbor at $\sim 100 - 200$ kpc away from O VI (Tripp et al. 2001; Tumlinson et al. 2005; Tripp et al. 2006), and the median distances of 200-270 kpc from $0.1 M^*$ galaxies derived by Stocke et al. (2006).

Stocke et al. (2006) stresses the need for deeper surveys below $0.1 L^*$ to find the galaxies responsible for the bulk of the IGM enrichment at low- z . Indeed, 66% of our intermediate absorbers neighbor $< 0.1 M^*$ galaxies, which is even

ing enrichment by low-metallicity or even Pop III stars are associated with weaker O VI lines, although this would be difficult as no other species has a similar transition in the UV. High- S/N observations of aligned C IV using COS could possibly probe similar low overdensities with the trend of derived $[\text{O}/\text{C}]$ with column density possibly indicating evolving nucleosynthetic yields.

⁷ It would be fascinating to see if nucleosynthetic yields indicat-

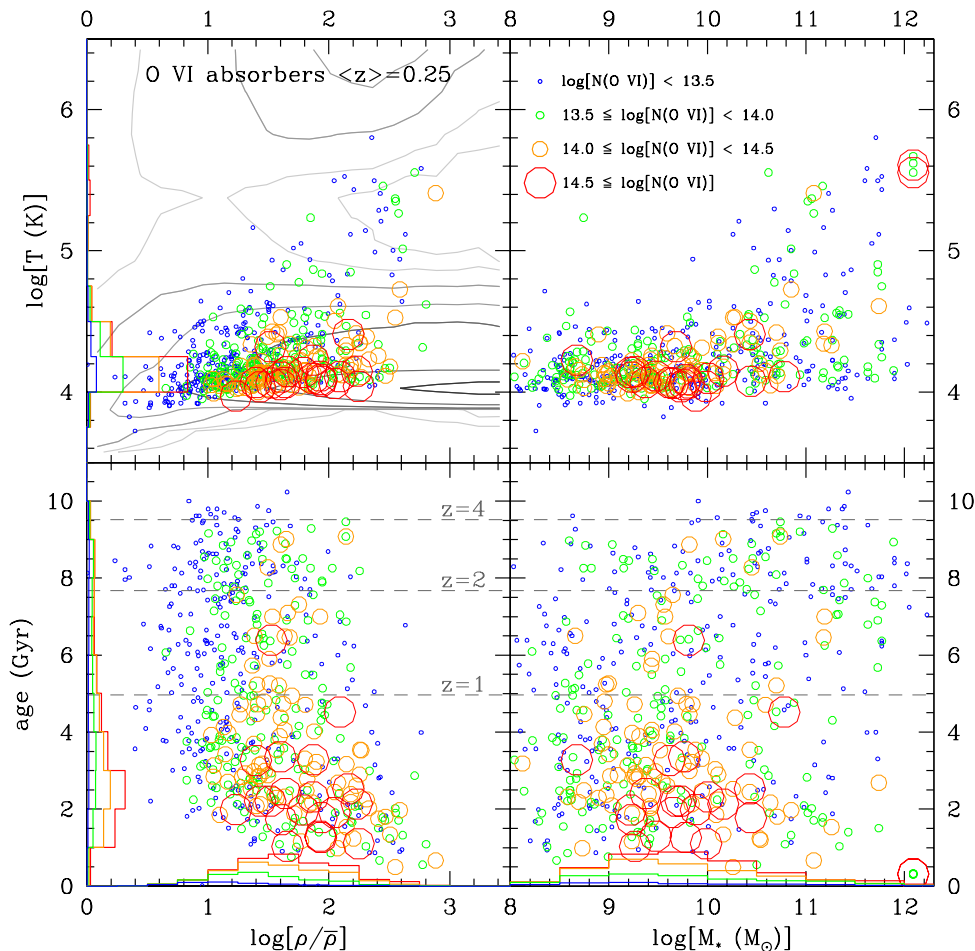


Figure 14. O VI absorbers from the high-quality d32n256vzw150-bturb sample are plotted in four phase space planes considering two physical parameters (O VI-weighted density and temperature), the age of gas tracing O VI absorbers (i.e. the time since the wind launch), and the stellar mass of the neighboring galaxy (i.e. the galaxy with the least fractional virial distance). Logarithmic contours at 0.5 dex steps in the $\rho - T$ phase space correspond to the metallicity-weighted density (lighter contours are less). O VI photo-ionized absorbers trace metals up to an overdensity (δ) of 300 where $f(\text{O VI})$ drops to almost zero, and O VI at higher density must be collisionally ionized. Few of these latter absorbers are found, because metals have a “zone of avoidance,” here due to efficient metal-line cooling through this region. Absorbers can be followed around the four panels by eye to see how these parameters are related to various O VI strengths. A density-age anti-correlation exists with O VI in CIE associated with recent activity, often in close proximity with M^* galaxies. Absorbers below $N(\text{O VI}) = 10^{14} \text{ cm}^{-2}$ do not correlate generally with environment showing little dependence on the neighboring M_{gal} . Such absorbers trace photo-ionized metals released in winds often at $z > 1$. Histograms along the side show the summed $\Sigma N(\text{O VI})$, with each color corresponding to the column density range indicated by the key in the upper right panel. Less than 10% of $\Sigma N(\text{O VI})$ is collisionally ionized.

more impressive considering our neighbor weighting scheme favors association with more massive galaxies. However, the ages of such absorbers are almost always greater than 2 Gyr, often much more, indicating that such association is perhaps incidental. The scenario may be related to C IV absorbers at $z \sim 2 - 3$ showing the same clustering at several comoving Mpc as Lyman-break galaxies (Adelberger et al. 2003, 2005), while Porciani & Madau (2005) find that this clustering arises even if the metals C IV traces were injected at very high- z . The same scenario appears to be in play for O VI absorbers, which often have little dynamical association with their neighboring galaxy and instead are injected at a much earlier epoch.

If O VI is not linked to its immediate environment, then perhaps this can explain Prochaska et al. (2006) finding 6 H I metal-free systems with qualitatively similar environmental

characteristics as their 6 systems with O VI along the PKS 0405-123 sight line; the O VI does not care about the immediate surroundings and therefore traces a wide range of environments. This supports the inhomogeneous nature of IGM metal enrichment, where O VI absorbers trace metals above the mean metallicity. We also find a significant fraction of our H I absorbers without aligned O VI (compare third and fourth rows of Figure 13).

As an aside, we plot the fraction of H I absorbers aligned with O VI as a function of column density at various δv separations in Figure 16, as long as O VI has an equivalent width $\geq 30 \text{ mÅ}$. Note that unlike O VI aligned with H I considered earlier, only one O VI component can be aligned with a single H I component. We provide this plot as a prediction for comparison with current and future data. We predict about half of $N(\text{H I}) = 10^{14.0} \text{ cm}^{-2}$ absorbers should have

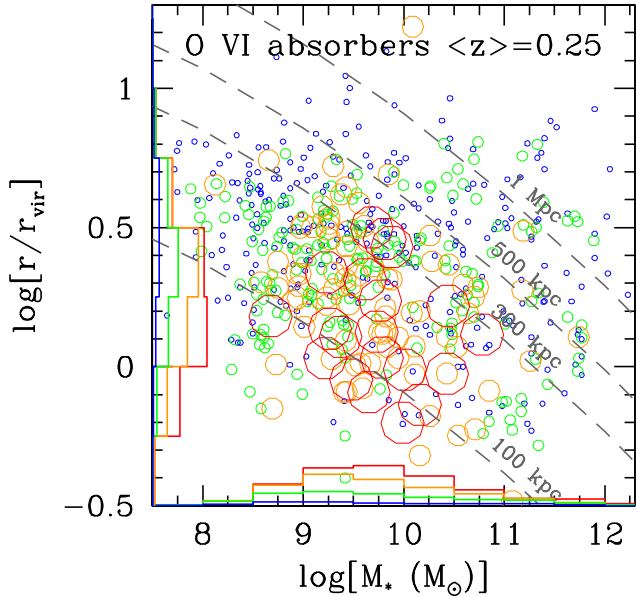


Figure 15. The distance to the neighboring galaxy, shown as a multiple of the virial radius, is plotted against that galaxy stellar mass for all O VI absorbers. The color and size key for O VI column density in Figure 14 applies here. Dashed lines show the physical distance assuming $z = 0.25$, and the colored histograms correspond to the number of absorbers in each O VI column density bin. Stronger O VI absorbers are more likely to be dynamically associated with more massive galaxies, with the strong absorbers almost always within $2 r_{\text{vir}}$. The range of physical distances seem similar to observed impact parameters. We obtain the virial radius by using the relation from Navarro, Frenk, & White (1997) for a dark matter halo; we convert from stellar to dynamical mass using the relation in the left center panel of Figure 1 of Davé (2009).

O VI within 80 km s^{-1} , however only 20% have well-aligned O VI. At $N(\text{H I}) = 10^{15-16} \text{ cm}^{-2}$, O VI lies within 80 km s^{-1} 88% of the time, but the simulations suggest such absorbers are slightly less likely to be well-aligned than the bin below it— a possible signature of O VI in CIE as we discuss next.

5.3 Collisionally Ionized O VI

The most obvious difference between collisionally ionized (CI) and photo-ionized (PI) O VI is environment. The few strong absorbers at CI temperatures in Figure 14 trace gas within or just outside halos of $\sim M^*$ galaxies undergoing rapid metal-line cooling in the metal “zone of avoidance.” Their relatively young ages, $\sim 0 - 2 \text{ Gyr}$, indicate association with recent enrichment. The strongest O VI absorber in PKS 1405-123 ($N(\text{O VI}) = 10^{14.8} \text{ cm}^{-2}$ at $z = 0.1671$) from Prochaska et al. (2006) fits this description almost perfectly; the O VI appears to be CI, nearly Z_{\odot} , and lies 108 kpc from a $4.1 L^*$ galaxy (i.e. $< r_{\text{vir}}$), which shows evidence for a burst of star formation $\sim 1 \text{ Gyr}$ ago. While Prochaska et al. (2006) expresses surprise no other galaxies lie near this absorber, we find this appropriate because our similar simulated absorbers depend predominantly on the environment associated with the parent halo; this is a clear contrast with PI absorbers in the diffuse IGM.

The strongest IGM O VI absorber yet observed at $z < 0.5$, the $N(\text{O VI}) = 10^{14.95} \text{ cm}^{-2}$ absorber in PKS 0312-

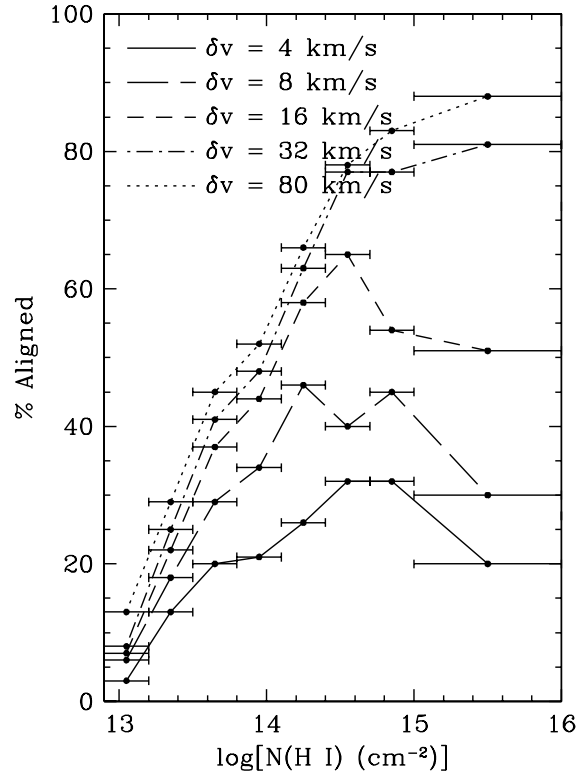


Figure 16. The alignment fraction of H I absorbers with O VI with at least $EW = 30 \text{ mÅ}$ at various δv 's using the d32n256vzw150-bturb model. Bins from $N(\text{H I}) = 10^{12.9-15.0} \text{ cm}^{-2}$ are 0.3 dex wide with the last bin spanning $N(\text{H I}) = 10^{15.0-16.0} \text{ cm}^{-2}$. Bins above $N(\text{H I}) = 10^{14.4} \text{ cm}^{-2}$ are much more likely to be aligned with O VI at some level. The strongest H I absorbers are associated 80% of the time with O VI, but are less likely to be well-aligned, which we suggest is a signature of O VI near or in halos more often collisionally ionized.

770, shows multi-phase behavior according to Lehner et al. (2008), where a PI Lyman limit system is aligned with O VI-bearing gas with a likely CI origin. This work finds an $0.7 L^*$ galaxy at an impact parameter of 38 kpc, with a morphology indicating a possible galaxy merger. Indeed, Lehner et al. (2008) interpret this system as possibly representing outflow materials cycling in a halo fountain as the impact parameter is consistent with a halo origin for this system.

We propose such CI O VI absorbers are primarily related to those observed in IVCs and HVCs (e.g. Savage et al. 2003; Sembach et al. 2003; Fox et al. 2006) associated with the MW halo or possibly the intragroup medium of the Local Group. This is consistent with the idea that CI O VI is the interface between a hot, tenuous halo medium at $T \geq 10^6$ and pressure-confined dense clumps of $\sim 5 \times 10^6 M_{\odot}$ proposed by Maller & Bullock (2004), and supported by the observations of the Lehner et al. (2008) system. The observed HVC $N(\text{O VI}) - b(\text{O VI})$ trend is also consistent with the Heckman et al. (2002) relation resulting from radiatively cooling flows of hot gases passing through the coronal temperature regime, yielding CI O VI.

One problem is that our absorbers are too strong; we find 14 very strong absorbers ($N(\text{O VI}) \geq 10^{15} \text{ cm}^{-2}$) over $\Delta z = 35$ while not one such absorber is found in any quasar sight lines or associated with the MW halo. Such absorbers

rarely occur and usually require CI O VI, because the path-lengths for PI O VI are too long. Our simulations are very under-resolved to adequately model such dense clumps using $m_{\text{SPH}} \sim 3 \times 10^7 M_{\odot}$. Halo O VI in CIE is likely to exist in many smaller structures creating weaker lines, which also may explain their wide b -parameters as one component is made up of many smaller parcels of gas at random, turbulent velocities. Hundreds or even thousands of SPH particles per $\sim 5 \times 10^6 M_{\odot}$ cloud are likely needed to model the large range of densities in pressure equilibrium.

Another reason for excessively strong CI O VI absorbers is possibly overestimated metallicities, assuming they are similar to MW HVCs. HVCs in general show metallicities of 0.1-0.3 Z_{\odot} (Tripp et al. 2003; Sembach et al. 2004b; Fox et al. 2005), with rare exceptions of super-solar HVCs near the galactic disk (e.g. Zech et al. 2008); conversely, our halo absorbers average Z_{\odot} . Our winds are confined in M^* halos recycling in halo fountains in a cycle less than a Gyr, which may be too fast. Again, resolution may be an issue as our single SPH particles fall straight through hot galactic halos, when they physically need to be pressure-confined. Two-phase boundaries in SPH are difficult as a particle shares a similar smoothing length and therefore density with its neighbors while it is at a very different temperature. Overestimated ram-pressure stripping reduces tangential velocities adding to this numerical artifact at the resolutions we explore (see Kereš et al. (2008) §4.3 for a discussion of this “cold drizzle”). If slower recycling is more realistic, fewer instances of metal enrichment occur, leading to lower metallicities while reducing our (overly high) star formation rates in massive galaxies. Accurate hydrodynamical modeling of O VI halo absorbers requires an increase of several orders of magnitude in resolution as well as non-equilibrium cooling and ionization. The non-equilibrium ionization fractions of Gnat & Sternberg (2007) may alleviate the overestimate of strong CI O VI absorbers by allowing lower $f(\text{O VI})$ at $T < 10^5$ K making more weak O VI halo absorbers with a larger filling factor.

Two characteristics of CI O VI are their multi-phase nature and their mis-alignment with H I. The multi-phase nature of O VI appears in observations showing coincident C III and strong H I in the strongest O VI absorbers (Prochaska et al. 2004; Danforth et al. 2006; Cooksey et al. 2008). Often our strongest absorbers show evidence that O VI itself is multi-phase, since such absorbers occupy temperatures in between PI and CI O VI (see the broad range of temperatures in the red histogram in the upper left panel of Figure 14). The CLOUDY tables we use require that absorbers where $10^{4.5} < T < 10^{5.3}$ K and $\delta > 100$ have multi-phase O VI since $f(\text{O VI})$ values are minuscule in this $\rho - T$ phase space.

The mis-alignment characteristic appears when we consider only simulated $N(\text{O VI})$ above $10^{13.5} \text{ cm}^{-2}$; such absorbers where $T > 10^5$ K are well-aligned ($\delta v \leq 8 \text{ km s}^{-1}$) only 36% of the time compared to 55% for lower temperature absorbers. Very mis-aligned absorbers ($\delta v > 80 \text{ km s}^{-1}$) occur 21% of the time for CI absorbers and only 12% for the cooler sample. The fact that only 7% of the T08 absorbers are what we consider very mis-aligned, including those without any H I at all, seems to support the case for predominantly PI O VI.

We note the analytical model of Furlanetto et al. (2005)

can explain all O VI as collisionally ionized when considering structural formation shocks propagating out to a $8 \times$ the virial radius. It is not straightforward to quantify how far our virial shocks propagate, but qualitatively from simulation animations⁸ it doesn't seem to propagate much beyond $2 r_{\text{vir}}$. Moreover, virial shocks don't carry metals as they propagate outwards. Finally, virial shocks at these distances are usually at low enough densities that the high ionization parameter makes O VI in CIE impossible; any O VI must be photo-ionized at lower temperatures. While Furlanetto et al. (2005) suggests an even split between CI and PI O VI if the shocks go to $4 r_{\text{vir}}$, our CI O VI is rarely found outside $2 r_{\text{vir}}$. Like them, we find strong absorbers should remain nearly unaffected by the extent of virial shocks considering none of our absorbers over $N(\text{O VI}) = 10^{14.7} \text{ cm}^{-2}$ lie outside of $2 r_{\text{vir}}$.

The frequency of our O VI systems with $N(\text{O VI}) \geq 10^{14.5} \text{ cm}^{-2}$ (i.e. summing all components within 100 km s^{-1}) is $1.8 \Delta z^{-1}$. We find a somewhat higher frequency of intersecting halos $\geq 0.1 M^*$ halos ($1.4 \Delta z^{-1}$ for $> M^*$ and $1.8 \Delta z^{-1}$ for $0.1 - 1 M^*$), however the frequency of a strong absorber within a virial radius of such galaxies occurs about a tenth of the time. While we find CI O VI relates to the immediate environment of a galaxy in a way PI O VI does not, not all strong absorbers are in CIE and more often trace gas within two virial radii around sub- M^* galaxies. A fascinating survey with COS would be to explore sight lines intersecting galactic halos for a range of galaxy masses and types ($\leq 150 \text{ kpc}$). The incidence of O VI as a function of impact parameter will provide a handle on the filling factor of O VI, which we suggest here is more often collisionally ionized within halos. A similar survey of C IV at $z < 1$ by Chen et al. (2001) finds a sharp cutoff above $\sim 100 \text{ kpc}$. However, strong O VI associated with H I does not imply that O VI is within the halo, as we have shown that the associated O VI often arises from lower overdensities outside. O VI may not have a similarly sharp cutoff at a specific impact parameter as C IV if this is the case.

To summarize, our simulations preliminarily suggest that the vast majority of O VI absorbers in quasar sight lines are likely photo-ionized. Our CI O VI fraction is less constrained; while we find a small fraction ($< 10\%$), this may increase if we could resolve the structures responsible for CI O VI, which we feel are related to the HVCs in our Galaxy and necessary to explain the strongest O VI systems. However, if we consider that CI O VI is associated with stronger absorbers, as other simulations also find (Cen et al. 2001; Fang & Bryan 2001), the steeper fit to the differential column density distribution ($d^2 n/dz dN(\text{O VI}) \propto N(\text{O VI})^{-2.0}$, DS08) compared to other species ($d^2 n/dz dN(\text{H I}) \propto N(\text{H I})^{-1.7}$, $d^2 n/dz dN(\text{C III}) \propto N(\text{C III})^{-1.8}$, also DS08) suggests there is not a large reservoir of CI O VI at high column densities. H I and C III have rising ionization fractions with higher density at PI temperatures; this is a clear contrast to $f(\text{O VI})$, which drops sharply at rising densities, possibly explaining part of the difference in the power law fits. Hence the CI versus PI O VI argument is not completely settled, but it seems very likely that most weak and intermediate O VI absorbers are photo-

⁸ See <http://luca.as.arizona.edu/~oppen/IGM/>

ionized, and that collisionally ionized O VI is usually associated with galactic halo gas.

5.4 COS Simulated Observations and Environment

As a prelude to the types of observations enabled by *Hubble*/COS, we consider O VI simulated absorption systems from a bright quasar continuum generated using the COS Spectral Simulator⁹ in Figure 17 where we assume 10,000 second integrations at all bands. Our point in this figure is to contrast the metal-line systems of PI and CI O VI absorbers to see how environment can lead to significant observational signatures. The PI O VI absorber with $b(\text{O VI}) = 35 \text{ km s}^{-1}$ at $z = 0.25$ is well-aligned ($\delta v = 0.9 \text{ km s}^{-1}$) with a H I component where $N(\text{H I}) = 10^{15.0} \text{ cm}^{-2}$ and $b(\text{H I}) = 47 \text{ km s}^{-1}$ from Ly β . This is a simple system with well-aligned C III and C IV tracing gas 195 kpc from a $10^{9.8} M_{\odot}$ galaxy ($4 r_{\text{vir}}$) with an average age of 4.4 Gyr and a metallicity of $0.45 Z_{\odot}$. We consider this absorber analogous to the $z = 0.20702$ absorber in HE 0226-4110 from Thom & Chen (2008b); their H I is slightly stronger and broken into two components although it appears centered on the O VI.

We show the density and temperature (mass-weighted) in the bottom two panels in physical space (blue) and velocity space (red). Peculiar velocities dominate over the spatial distribution even in a PI absorber tracing the diffuse IGM. At the line center different parcels of gas overlap resulting in a multi-phase PI absorber ($T(\text{O VI}) = 10^{4.1} \text{ K}$ & $T(\text{H I}) = 10^{4.3} \text{ K}$; $\delta(\text{O VI}) = 47$ & $\delta(\text{H I}) = 86$). In this case, gas from surrounding voids accreting into the local filament heats the extended gas extending $\sim 1 \text{ Mpc}$ around the galaxy to $T \sim 10^{5.2} \text{ K}$. This gas is mostly unenriched, despite being at CIE temperatures; any oxygen present would be photo-ionized to a higher state at such low density anyway. This suggests that there may be considerable WHIM gas that cannot be traced by any metal lines, owing to the small filling factor of metals in the IGM.

To demonstrate a typical CI O VI absorber, we show a $10^{14.2} \text{ cm}^{-2}$ component, which happens to be aligned with a weak BLA ($N(\text{H I}) = 10^{13.5} \text{ cm}^{-2}$, $b(\text{H I}) = 50 \text{ km s}^{-1}$). In contrast to the type of simple aligned absorbers T08 observes, which indicate photo-ionization, the H I distribution here is multi-component, extended, and weaker (another $10^{13.5} \text{ cm}^{-2}$ H I component lies 80 km s^{-1} away). This system is multi-phase with $T(\text{O VI}) = 10^{5.01} \text{ K}$ indicating possibly some weak aligned PI O VI, while $T(\text{H I}) = 10^{4.16} \text{ K}$. BLAs usually do *not* primarily trace gas at temperatures above 10^5 K , often because aligned $T = 10^4 \text{ K}$ gas dominates the absorption. Lying 270 kpc from a massive $10^{11.5} M_{\odot}$ galaxy, this system traces gas with $Z = 0.45 Z_{\odot}$ in the intragroup medium just outside of the halo. Unlike most other CI absorbers, which are often stronger, the metals traced are older, 6.6 Gyr. An observed analog may be the $z = 0.1212$ system in H1821+643, which indicates CI O VI (Tripp et al. 2001), although the associated H I is somewhat stronger and broader in that system.

As an example of extreme multi-phase behavior, we show another system in Figure 18. Although the CI absorber

at $z = 0.36$ is the same column density and has nearly the same metallicity as the PI absorber in Figure 17, almost everything else about it is different. The absorber is wider, $b(\text{O VI}) = 51 \text{ km s}^{-1}$, and is paired with a component 103 km s^{-1} away ($N(\text{O VI}) = 14.4 \text{ cm}^{-2}$ & $b(\text{O VI}) = 47 \text{ km s}^{-1}$). The main absorber is clearly in CIE, $T(\text{O VI}) = 10^{5.45} \text{ K}$ at $\delta(\text{O VI}) = 350$, and is slightly more than $1 r_{\text{vir}}$ (195 kpc) away from a $10^{11.1} M_{\odot}$ galaxy; this indicates the absorber arises in the intragroup medium with ages of $\sim 2 \text{ Gyr}$. Peculiar velocities of several hundred km s^{-1} heavily confuse the spatial distribution, creating one of the most extreme multi-phase absorbers in our sample. This is a Lyman limit system, $N(\text{H I}) = 10^{17.9} \text{ cm}^{-2}$, only because of a chance alignment with the ISM of a dwarf galaxy ($M_{\text{gal}} = 10^{8.9} M_{\odot}$) centered only 5 kpc from the line of sight. In our sample of $\Delta z = 35$, this is the H I absorber closest to any galaxy tracing the highest overdensity, $\delta(\text{H I}) = 5 \times 10^4$, and is completely coincidental. Self-shielding may raise $N(\text{H I})$ substantially, but almost any other line of sight passing through this region would intersect the more extended intragroup O VI and probably be mis-aligned with a much weaker BLA tracing halo or intragroup gas. The lower ionization metal species arise primarily from the dwarf galaxy ISM. This absorber is similar to the $z = 0.2028$ absorber observed in PKS 0312-770 by Lehner et al. (2008), although in that case the Lyman limit system is possibly co-spatial with the O VI-bearing gas and not the ISM of a separate galaxy.

The type of simulation analysis demonstrated here for these three systems should provide a prelude to a future direction in using simulations for metal-line absorber modeling. Hydrodynamical simulations are necessary to model the complex environment and peculiar velocity field, the apparently inhomogeneous distribution of metals, and eventually the ionization conditions resulting from spatially and temporally non-uniform ionization sources. The first challenge is to be able to accurately simulate the complex low- z systems observed by STIS and soon COS, and the second is to understand the physical and evolutionary processes within the simulations with an emphasis on environmental context.

Our simulations appear to be able to generate such complex absorbers, however we admit that we have to search over a pathlength of $\Delta z = 35$ to find just the right CI absorbers that reproduce the properties of some of the most well-studied low- z O VI systems found among lines of sight covering a much smaller path length. Accurate self-consistent hydrodynamical modeling, especially in CI absorbers, appears to be a ways away, requiring several order of magnitude of improved resolution, radiative transfer, and non-equilibrium effects. We are more confident about our ability to model the PI absorbers tracing the diffuse enriched IGM, but we only display one, as these are a fairly homogeneous population.

As for environment, we have only taken a first step in that direction when considering the mass and distance to the neighboring galaxy and the age of the absorber. The characteristics of the originating galaxy, the velocity it was launched at, the number of times a metal has been recycled, and the spread in ages of metals within an absorber are just a few of the things we have considered here. Such considerations are more informative for photo-ionized O VI because these absorbers appear to be relatively unrelated to their neighboring galaxy.

⁹ <http://arlsrv.colorado.edu/cgi-bin/ion-p?page=ETC.ion>

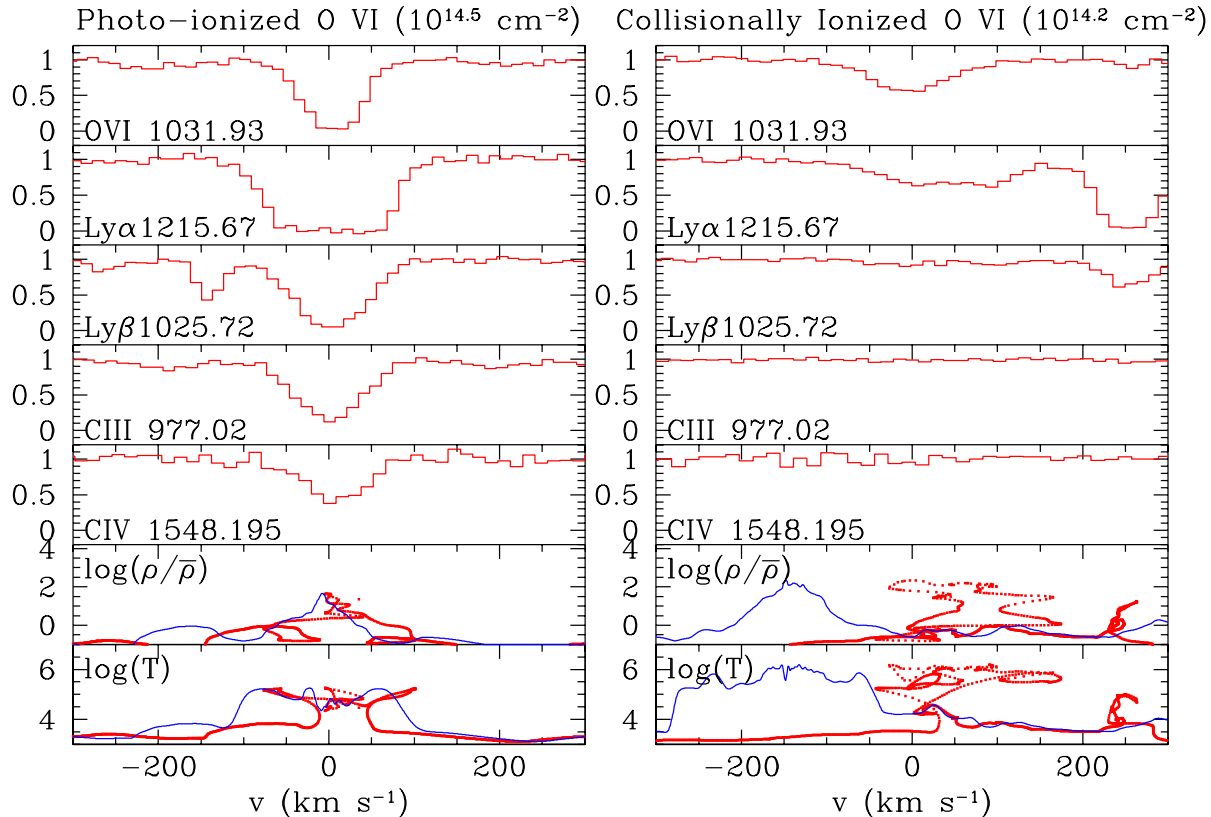


Figure 17. Two metal-line systems simulated at prospective COS resolution and S/N . Absorption lines and physical parameters plotted in red are in velocity space, while blue indicates the spatial distribution of density and temperature in the bottom two panels without peculiar velocities. The left system at $N(\text{O VI}) = 10^{14.5} \text{ cm}^{-2}$ is comprised of photo-ionized gas well-aligned with H I at $N(\text{H I}) = 10^{15.0} \text{ cm}^{-2}$ tracing gas 195 kpc from a $\sim 0.1 M^*$ galaxy. The right system is a $10^{14.2} \text{ cm}^{-2}$ O VI absorber in CIE lying 270 kpc from a super- M^* galaxy showing a weak asymmetric H I profile and no lower-ionization metals lines. Both absorbers have metallicities of $0.45 Z_{\odot}$. Peculiar velocities dominate over spatial distribution of metals and baryons as in the systems. The two systems, comparable to actual observed systems, emphasize the different environments from which O VI absorbers arise.

6 SUMMARY

We examine the nature and origin of O VI absorbers in the low redshift ($z < 0.5$) IGM using GADGET-2 cosmological hydrodynamic simulations including outflows, exploring a variety of wind models and input physics variations. We determine the best-fitting model by comparing to a suite of observed O VI and H I absorber statistics, including the cumulative equivalent width distribution, $b(\text{O VI})$ as a function of $N(\text{O VI})$, and the $N(\text{O VI})$ as a function of $N(\text{H I})$.

Our first main result is that *only a model where we explicitly add sub-resolution turbulence is able to match all observations*. The observations motivating this conclusion are the progressively larger line widths for stronger O VI systems, along with the high incidence of large equivalent width absorbers. We discuss this further later on.

The second main result is that *the vast majority of O VI absorbers are photo-ionized, with only a few strong systems being collisionally ionized*. This result does not depend on turbulence or any other input physics variations. The governing variable in photo-ionized O VI strength is density, which steadily increases from overdensities of ~ 10 for the weakest observed absorbers tracing metals in extended filaments, to ~ 200 for the strongest observed absorbers tracing metals in or around galactic halos. Increasing metallic-

ity with density also helps O VI column densities become stronger.

Our third main result is that *metals in the IGM are distributed inhomogeneously, and that O VI absorbers preferentially arise from over-enriched regions*. The average absorber traces metals $5\times$ above the mean metallicity-density relationship in our simulation ($0.15 - 1.0 Z_{\odot}$). Only 1.3% of the IGM volume enriched to greater than $0.1 Z_{\odot}$, with a filling factor of only 0.3% resulting from weaker winds working nearly as well. We also test a uniform distribution of IGM metals, finding that this creates too many weak absorbers. Our results imply that applying the mean IGM metallicity-density gradient to gas everywhere in order to study metal absorption is not appropriate; the *scatter* in the global metallicity-density relationship critically influences O VI absorbers.

The clumpy metal distribution is an important reason why most O VI is at photo-ionization temperatures, because it strongly enhances metal-line cooling. Oxygen is a powerful coolant and is (not coincidentally) particularly efficient in the narrow temperature regime where O VI has a collisional ionization maximum. This creates a “zone of avoidance” for enriched IGM gas between $10^{4.5} - 10^{5.5} \text{ K}$. Previous theoretical studies that did not account for metal line cooling incorrectly predict more collisionally ionized sys-

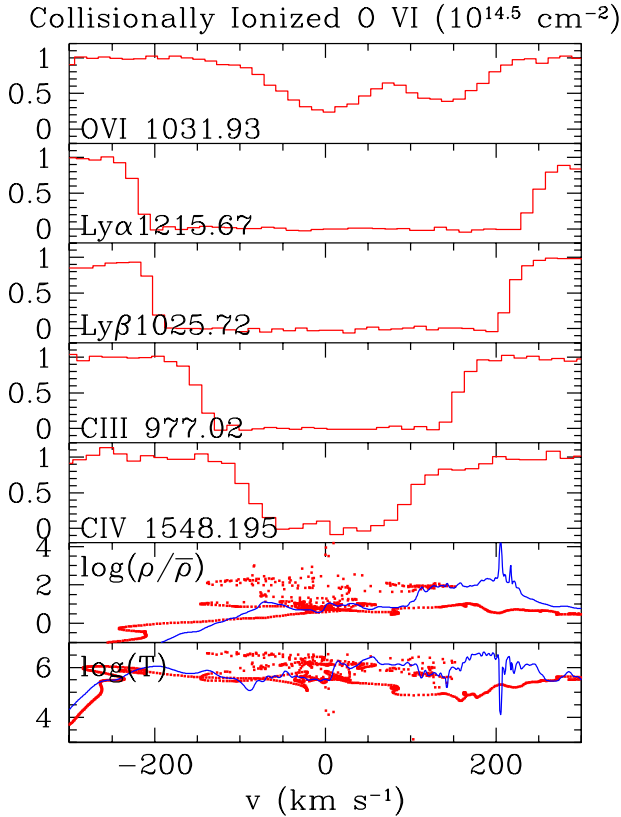


Figure 18. Centered on a $10^{14.5} \text{ cm}^{-2}$ O VI component in CIE, this multi-component system is a result of O VI in the intragroup medium 195 kpc from a M^* galaxy aligned with a Lyman limit system $N(\text{H I}) = 10^{17.9} \text{ cm}^{-2}$ arising from a chance alignment with the ISM of a nearby dwarf galaxy, $M_{\text{gal}} = 10^{8.9} M_{\odot}$, which is also responsible for the strong C III and C IV. Overlapping gas in velocity space aligns H I gas at 10^4 K with O VI gas at 10^5 K .

tems. Non-equilibrium ionization allows collisionally ionized O VI to extend to lower temperatures (Gnat & Sternberg 2007), but the differences are only important for relatively rare high density regions, and do little to alter the overall O VI statistics. The high fraction of aligned absorbers in the Thom & Chen (2008a) and Tripp et al. (2008) datasets supports most O VI absorbers being photo-ionized. While observed complex, multi-phase systems with mis-aligned components indicating CIE O VI may be under-represented in our simulations, it is unlikely that would dominate typical O VI systems under any circumstance. A key implication of our findings is that *O VI is generally a poor tracer of the Warm-Hot Intergalactic Medium (WHIM), and cannot be used to infer the WHIM baryonic content.*

In depth study of the properties of O VI absorbers and their associated H I reveals that multi-phase temperatures and densities are often needed to explain their properties. Metal-line cooling allows inhomogeneously distributed O VI to cool slightly below H I-weighted temperatures, while stronger O VI absorbers often trace lower overdensities than aligned strong H I, which typically traces gas inside halos. Such a multi-density photo-ionized model appears necessary to explain strong O VI absorbers aligned with $N(\text{H I}) > 10^{15} \text{ cm}^{-2}$ when considering absorbers on the $N(\text{H I}) - N(\text{O VI})$ plane. The Tripp et al. (2008) dataset finds

more weak H I absorbers aligned with O VI than our simulations, possibly indicating local fluctuations in the meta-galactic photo-ionizing background around 1 Rydberg.

We find good agreement with observations for the distribution of velocity separations between O VI and H I absorbers. The typical length of a photo-ionized O VI absorber is 50 – 100 kpc, although the peculiar velocity field often dominates resulting in mis-aligned H I components, especially those tracing higher densities. Only 42% of our strong absorbers $N(\text{O VI}) \geq 10^{14} \text{ cm}^{-2}$ are aligned within 4 km s^{-1} while 91% are aligned within 80 km s^{-1} . This indicates a clumpy distribution of O VI that does not exactly trace the smoothly varying gas in the Ly α forest, but still arises in the same underlying large-scale structure.

A clear anti-correlation exists between the density traced by O VI and its age as determined by the last time the metals were launched in a wind. This trend arises in our simulations because of the outside-in pattern of metal enrichment; outer, lower overdensities are enriched first when the Universe is young and physical distances are small, and inner, higher overdensities are progressively more enriched by later winds extending a smaller comoving distance. This is a consequence of our finding in Oppenheimer & Davé (2008) that winds travel similar physical distances relatively independent of redshift or galaxy mass. While a majority of metals falls back into galaxies, our work here shows that low- z O VI absorbers below $N(\text{O VI}) \sim 10^{14} \text{ cm}^{-2}$ provide one of the best ways to observe the oldest metals that remain in the IGM. We suggest the fascinating possibility of deriving nucleosynthetic yields tracing the earliest stars if another high ionization species, such as C IV, can be observed at low densities with the increased throughput of COS or future facilities.

Finally, we study the galaxy environment around O VI absorbers. Photo-ionized O VI usually has little to do with either the mass of the neighboring galaxy, averaging $\sim 0.03 - 0.1 M^*$, or the distance, averaging $\gtrsim 2 r_{\text{vir}}$, because of the significant galactic and large-scale structural evolution occurring while these metals reside in the IGM. This helps explain why observed photo-ionized absorbers appear to trace a variety of environments, with a typical distance of 100-300 kpc to the nearest galaxy. The opposite is true of the small minority of collisionally ionized absorbers. These strong absorbers are $< 2 r_{\text{vir}}$ from M^* galaxies and have ages indicating activity within the last 2 Gyr, and are perhaps analogous to O VI observed in HVCs and IVCs in the Milky Way halo. The relatively young age for strong O VI signifies that these metals recycle back into galaxies multiple times in what can be described as halo fountains (Oppenheimer & Davé 2008).

The most uncertain and controversial part of this paper is the claim that significant sub-resolution turbulence is present in O VI absorbers. We determine the amount of turbulence needed by directly fitting the observed $N(\text{O VI}) - b(\text{O VI})$ relation. This increases b -parameters to observed levels by construction, while simultaneously increasing large- EW absorbers to the observed frequency. We attempt to justify this “magic bullet”, as well as compare the implied turbulence to other instances of observed IGM turbulence. We point out that various authors have argued for clumpiness in IGM metals extending well below the mass and spatial resolution of our simulations (Simcoe et al. 2006; Schaye et al. 2007). If such clumpiness exists, then surely

those clumps must have some relative motion, so assuming completely static velocities below the SPH smoothing scale of 20 – 100 kpc is unrealistic. Our model states that strong absorbers can be dominated by turbulent motions, just as the line profiles associated with molecular clouds, H II regions, IVCs, and HVCs associated with our Galaxy are. The energy dissipation required using a Kolmogorov spectrum is a fraction of the turbulence observed by Rauch et al. (2001) in high- z C IV absorbers, which is encouraging considering the IGM at late times should be calmer, although it is unclear whether Kolmogorov theory accurately describes IGM turbulence. We show that this trend is quantitatively consistent with the idea that turbulence dissipates as metals reside longer in the IGM. Our turbulent scenario makes the case that metal-line absorbers are made up of numerous cloudlets with lower ionization species tracing high-density clouds making multiple thin profiles, and O VI tracing more of the low-density regions in between creating a single broader profile; such is often observed to be the structure of low- z metal line systems. In short, we believe that small-scale turbulence is a viable possibility, although more detailed modeling is required to fully understand its implications. Applying a volume renormalization zoom technique to cosmological simulations, allowing the resampling of individual haloes in galactic-scale simulations, provides a realistic, near-term possibility for following the evolution of turbulence over a Hubble time.

While it may be disappointing that O VI is a poor WHIM tracer and provides only a weak handle on the IGM metal distribution, our results open up some new and interesting possibilities for using O VI absorbers to understand cosmic metals and feedback. For instance, low- z O VI may provide a fascinating opportunity to study some of the oldest IGM metals in the Universe through weak absorbers. The strongest absorbers appear related to the recycling of gas between the IGM and galaxies, providing a unique window into how galaxies get their gas (e.g. Kereš et al. 2005, 2008). Detecting multiple ions in weaker absorbers will provide a good handle on physical conditions owing to the photo-ionized nature of O VI. Our work here is only a first step towards understanding the nature and origin of O VI in the low- z Universe using numerical simulations, which we hope to extend further by considering other metal species in a greater evolutionary context. We stress the need to model in detail the complex metal-line systems that will undoubtedly be observed by COS. The computational models presented, while state of the art, still fall well short of what is necessary, particularly for stronger collisionally ionized systems. We anticipate that future observational and modeling improvements will shed new light on the metal distribution at the present cosmic epoch with all its important implications. This work provides a first step in that direction.

ACKNOWLEDGMENTS

We thank Todd Tripp for inspirational conversations that helped spur this investigation in the first place. Valuable conversations with Blair Savage, Nicolas Lehner, Christopher Thom, and Hsiao-Wen Chen provided useful guidance. Support for this work was provided by NASA through grant number HST-AR-10946 from the SPACE TELESCOPE

SCIENCE INSTITUTE, which is operated by AURA, Inc. under NASA contract NAS5-26555. Support for this work, part of the Spitzer Space Telescope Theoretical Research Program, was also provided by NASA through a contract issued by the Jet Propulsion Laboratory, California Institute of Technology under a contract with NASA. Support was also provided by the National Science Foundation through grant number DMS-0619881.

REFERENCES

- Adelberger, K. L., Steidel, C. C., Shapley, A. E., & Pettini, M. 2003, *ApJ*, 584, 45
- Adelberger K. L., Shapley A. E., Steidel C. C., Pettini M., Erb D. K., & Reddy N. A. 2005, *ApJ*, 629, 636
- Anders, E. & Grevesse, N. 1989, *Geochim. Cosmochim. Acta*, 53, 197
- Asplund M., Grevesse N., & Sauval A. J., 2005, in Barnes T. G. III, Bash F. N., eds, *ASP Conf. Ser. Vol. 336. Cosmic Abundances as Records of Stellar Evolution and Nucleosynthesis*. Astron. Soc. Pac., San Francisco, p. 25
- Bahcall, J. N., Jannuzi, B. T., Schneider, D. P., Hartig, G. F., Bohlin, R., & Junkkarinen, V. 1991, *ApJ*, 377, L5
- Bertone, S. & White, S. D. M. 2006, *MNRAS*, 367, 247
- Cen, R. & Ostriker, J. P., 1999, *ApJ*, 514, 1
- Cen, R., Tripp, T. M., Ostriker, J. P., Jenkins, E. B. 2001, *ApJL*, 559, L5
- Cen, R. & Ostriker, J. P. 2006, 650, 560
- Cen, R. & Fang, T. 2006, *ApJ*, 650, 573
- Chen, H.-W., Lanzetta, K. M., & Webb, J. K. 2001, *ApJ*, 556, 158
- Chen, X., Weinberg, D. H., Katz, N., & Davé, R. 2003, *ApJ*, 594, 42
- Cole, S. et al. 2001, *MNRAS*, 326, 255
- Cooksey, K. L., Prochaska, J. X., Chen, H.-W., Mulchaey, J. S., & Weiner, B. J. 2008, *ApJ*, 676, 262
- Croft, R. A. C., Weinberg, D. H., Katz, N., & Hernquist, L. 1998, *ApJ*, 495, 44
- Danforth, C. W., Shull, M. J. 2005, *ApJ*, 624, 555
- Danforth, C. W., Shull, M. J., Rosenberg, J. L., & Stocke, J. T. 2006, *ApJ*, 640, 716
- Danforth, C. W. & Shull, M. J. 2008, *ApJ*, 679, 194 (DS08)
- Davé, R., Hernquist, L., Weinberg, D. H., & Katz, N. 1997, *ApJ*, 477, 21
- Davé, R., Hellsten, U., Hernquist, L., Katz, N., & Weinberg, D. H. 1998, *ApJ*, 509, 661
- Davé, R., Hernquist, L., Katz, N., & Weinberg, D. H. 1999, *ApJ*, 511, 521
- Davé, R. et al. 2001, *ApJ*, 552, 473
- Davé, R. & Tripp, T. M. 2001, *ApJ*, 553, 528
- Davé, R. & Oppenheimer, B. D. 2006, *MNRAS*, 374, 427
- Davé, R., Oppenheimer, B. D., & Sivanandam, S. 2008, *MNRAS*, 391, 110
- Davé, R. 2009, *astro-ph/arXiv:0901.3149*
- Erb, D. K., Shapley, A. E., Pettini, M., Steidel, C. C., Reddy, N. A., & Adelberger, K. L. 2006, *ApJ*, 644, 813
- Fang, T. & Bryan, G. L. 2001, *ApJ*, 561, L31
- Fechner, C. & Reimers, D. 2007, *A&A*, 463, 69
- Ferland, G. J., Korista, K. T., Verner, D. A., Ferguson, J. W., Kingdon, J. B., & Verner, E. M. 1998, *PASP*, 110, 761

- Finlator, K. & Davé, R. 2008, MNRAS, 385, 2181
- Fox, A. J., Savage, B. D., Wakker, B. P., Richter, P., Sembach, K. R., & Tripp, T. M. 2004, ApJ, 602, 738
- Fox, A. J., Wakker, B. P., Savage, B. D., Tripp, T. M., Sembach, K. R., & Bland-Hawthorn, J. 2005, ApJ, 630, 332
- Fox, A. J., Savage, B. D., & Wakker, B. P. 2006, ApJS, 165, 229
- Frank, S., Bentz, M. C., Stanek, K. Z., Mathur, S., Dietrich, M., Peterson, B. M., & Atlee, D. W. 2007, Ap&SS, 312, 325
- Fujita, A., Martin, C. L., Mac Low, M.-M., New, K. C. B., & Weaver, R. 2008, astro-ph/0803.2892, submitted to ApJ
- Fukugita, M., Hogan, C. J., & Peebles, P. J. E. 1998, ApJ, 503, 518
- Fukugita, M. & Peebles, P. J. E. 2004, ApJ, 616, 643
- Furlanetto, S., Phillips, L. A., & Kamionkowski, M. 2005, MNRAS, 359, 295
- Ganguly, R., Cen, R., Fang, T., & Sembach, K. 2008, ApJ, 678L, 89
- Gnat, O. & Sternberg, A. 2007, ApJS, 168, 213
- Haardt, F. & Madau, P. 2001, in “Clusters of galaxies and the high redshift universe observed in X-rays, Recent results of XMM-Newton and Chandra”, XXXVIth Rencontres de Moriond, eds. D.M. Neumann & J.T.T. Van.
- Hao H. et al., 2007, ApJ, 659, L99
- Heckman, T. M., Norman, C. A., Strickland, D. K., & Sembach, K. R. 2002, ApJ, 577, 691
- Hinshaw, G. 2008 astro-ph/0803.0732, accepted to ApJS
- Impey, C. D., Petry, C. E., Malkan, M. A., & Webb, W. 1996, ApJ, 463, 473
- Janknecht, E., Reimers, D., Lopez, S., & Tytler, D. 2006, A&A, 458, 427
- Joung, M. R. & Mac Low, M.-M. 2006, ApJ, 653, 1266
- Joung, M. R., Mac Low, M.-M. & Bryan, G. L. 2008, astro-ph/0811.3747
- Kereš, D., Katz, N., Weinberg, D. H., & Davé, R. 2005, MNRAS, 363, 2
- Kereš, D., Katz, N., Fardal, M., Davé, R., & Weinberg, D. H. 2008, astro-ph/0809.1430, accepted to MNRAS
- Kolmogorov A. N., 1941, Doklady Akad. Nauk SSSR, 30, 301
- Larson R. B., 1981, MNRAS, 194, 809
- Lehner, N., Savage, B. D., Wakker, B. P., Sembach, K. R., & Tripp, T. M. 2006, ApJS, 164, 1
- Lehner, N., Savage, B. D., Richter, P., Sembach, K. R., Tripp, T. M., & Wakker, B. P. 2007, ApJ, 658, 680
- Lehner, N., Prochaska, J. X., Kobulnicky, H. A., Cooksey, K. L., Howk, J. C., Williger, G. M., & Cales, S. L. 2008, astro-ph/0812.4231, accepted to ApJ
- Limongi, M. & Chieffi, A. 2005, ASP Conference Series, Vol. 342, 1604-2004: Supernovae as Cosmological Light-houses, Astron. Soc. Pac., San Francisco, p.122
- Lopez, S., Ellison, S., D’Odorico, S., & Kim, T.-S. 2007, A&A, 469, 61
- Mac Low M.-M. & Klessen R. S. 2004, Rev. Mod. Phys., 76, 125
- Maller, A. H. & Bullock, J. S. 2004, MNRAS, 355, 694
- Martin, C. L. 2005, ApJ, 621, 227
- Murray, N., Quatert, E., & Thompson, T. A. 2005, ApJ, 618, 569
- Navarro, J. F., Frenk, C. S., & White, S. D. M. 1997, ApJ, 490, 493
- O’Dell, C. R. 1991, in IAU Symp. 147, Fragmentation of Molecular Clouds and Star Formation, ed. E. Falgarone et al. (San Francisco: ASP), 476-479
- Oppenheimer, B. D. & Davé, R. A. 2006, MNRAS, 373, 1265 (OD06)
- Oppenheimer, B. D., Davé, R., & Finlator, K. 2007 EAS, 24, 157
- Oppenheimer, B. D. & Davé, R. 2008, MNRAS, 387, 587 (OD08)
- Oppenheimer, B. D., Davé, R., & Finlator, K. 2009, astro-ph/0901.0286, submitted to MNRAS
- Paschos, P., Jena, T., Tytler, D., Kirkman, D., & Norman, M. L. 2008, astro-ph/0802.3730
- Penton, S. V., Stocke, J. T., & Shull, J. M. 2004, ApJ, 152, 29
- Porciani, C. & Madau, P. 2005, ApJ, 625, L43
- Prochaska, J. X., Chen, H.-W., Howk, J. C., Weiner, B. J., & Mulchaey, J. 2004, ApJ, 617, 718
- Prochaska, J. X., Weiner, B. J., Chen, H.-W., & Mulchaey, J. S. 2006, ApJ, 643, 680
- Rauch, M., Sargent, W. L. W., & Barlow, T. A. 1999, ApJ, 515, 500
- Rauch, M., Sargent, W. L. W., & Barlow, T. A. 2001, ApJ, 554, 823
- Richter, P., Savage, B. D., Tripp, T. M., & Sembach, K. R. 2004, ApJS, 153, 165
- Richter, P., Fang, T., & Bryan, G. L. 2006, A&A, 451, 767
- Savage, B. D., Sembach, K. R., Tripp, T. M., & Richter, P. 2002, ApJ, 564, 631
- Savage, B. D., Sembach, K. R., Wakker, B. P., Richter, P., Meade, M., Jenkins, E. B., Shull, J. M., Moos, H. W., & Sonneborn, G. 2003, ApJS, 146, 125
- Schaye, J. 2001, ApJ, 559, 507
- Schaye, J., Carswell, R. F., & Kim, T.-S. 2007, MNRAS, 379, 1169
- Sembach, K. R., Wakker, B. P., Savage, B. D., Richter, R., Meade, M., Shull, J. M., Jenkins, E. B., Sonneborn, G., & Moos, H. W. 2003, ApJS, 146, 165
- Sembach, K. R., Tripp, R. M., Savage, B. D., & Richter, P. 2004, ApJS, 155, 351
- Sembach, K. R. et al. 2004, ApJS, 150, 387
- Simcoe, R. A., Sargent, W. L. W., Rauch, M., & Becker, G. 2006, ApJ, 637, 648
- Springel, V. & Hernquist, L. 2003, MNRAS, 339, 312
- Springel, V. 2005, MNRAS, 364, 1105
- Stoeke, J. T., Penton, S. V., Danforth, C. W., Shull, J. M., Tumlinson, J., & McLin, K. M. 2006, ApJ, 641, 217
- Sutherland, R. S. & Dopita, M. A. 1993, ApJS, 88, 253
- Thom, C. & Chen, H.-W. 2008a, ApJ, 683, 22
- Thom, C. & Chen, H.-W. 2008b, ApJS, 179, 37
- Tremonti, C. A. et al. 2004, ApJ, 613, 898
- Tripp, T. M., & Savage, B. D. 2000, ApJ, 542, 42
- Tripp, T. M., Savage, B. D., & Jenkins, E. B. 2000, ApJ, 534, L1
- Tripp, T. M., Giroux, M. L., Stocke, J. T., Tumlinson, J., & Oegerle, W. R. 2001, ApJ, 563, 724
- Tripp, T. M. et al. 2003, AJ, 125, 3122
- Tripp, T. M., Aracil, B., Bowen, D. V., & Jenkins, E. B. 2006, ApJ, 643, L77

- Tripp, T. M., Sembach, K. R., Bowen, D. V., Savage, B. D., Jenkins, E. B., Lehner, N., & Richter, P. 2008, ApJS, 177, 39 (T08)
- Tumlinson, J., & Fang, T. 2005, ApJ, 623, L97
- Tumlinson, J., Shull, M. J., Giroux, M. L., & Stocke, J. T. 2005, ApJ, 620, 95
- Weymann, R. J. et al. 1998, ApJ, 506, 1
- Yoshida, N., Furlanetto, S. R., & Hernquist, L. 2005, ApJ, 618, L91
- Zech, W. F., Lehner, N., Howk, J. C., Dixon, W. V. D., & Brown, T. M. 2008, ApJ, 679, 460
- Zheng et al. 2004, ApJ, 605, 631